Special Section: Coupled Surface–Subsurface Modelinge

Vadose Zone Journal

A Second-Order Accurate, Finite Volume–Based, Integrated Hydrologic Modeling (FIHM) Framework for Simulation of Surface and Subsurface Flow

Mukesh Kumar,* Christopher J. Duffy, and Karen M. Salvage

Surface water, the vadose zone, and groundwater are linked components of a hydrologic continuum. In order to capture the interaction between different components of a hydrologic continuum and to use this understanding in water management situations, an accurate numerical model is needed. The quality of model results depends on accurate representation of the physical processes and the data describing the area of interest, as well as performance of the numerical formulation implemented. Here we present a physics-based, distributed, fully coupled, second-order accurate, upwind cell-centered, constrained unstructured mesh based finite-volume modeling framework (FIHM) that simultaneously solves two-dimensional unsteady overland flow and three-dimensional variably saturated subsurface flow in heterogeneous, anisotropic domains. A multidimensional linear reconstruction of the hydraulic gradients (surface and subsurface) is used to achieve second-order accuracy. Accuracy and efficiency in raster data and vector-boundary representations are facilitated through the use of constrained Delaunay meshes in domain discretization. The experiments presented here (i) explore the influence of initial moisture conditions, soil properties, anisotropy, and heterogeneity in determining the pressure head distributions in the vadose and saturated zones, (ii) show the existence of localized "flux rotation" phenomenon due to heterogeneous anisotropy, leading to the creation of convergence–divergence zones, (iii) show the influence of vertical drainage from unsaturated zone on the response of an unconfined aquifer to pumping, and (iv) show the effects of capillarity, saturation excess, infiltration excess, and initial water table location on determining the overland flow generation.

Abbreviations: CVFE, control volume finite element; FIHM, finite volume-based integrated hydrologic modeling; GIS, geographical information system; ODE, ordinary differential equation; PDE, partial differential equation.

Understanding and predicting of flow on the surface and in the subsurface necessitates recognizing "that surface water and ground water are simply two manifestations of a single integrated resource" (Winter et al., 1998). This recognition has stimulated the development of numerical models capable of simulating the interactions between surface and subsurface flow. The accuracy of the simulation relies heavily on (i) the choice of governing equations used to simulate a flow behavior (e.g., three-dimensional Richards' equation for subsurface flow), (ii) the numerical methodology chosen to solve the governing equations (e.g., finite difference or volume) and the order of its accuracy, (iii) the accuracy of representation of hydrogeologic data on the model grids (details in Kumar, 2009), and finally, (iv) the discretization methodology (unstructured or structured mesh) and its resolution. Coupled surface–subsurface models include InHM (VanderKwaak, 1999), MIKE SHE (Graham and Refsgaard, 2001), WASH123D (Yeh and Huang, 2003), MODHMS (Panday and Huyakorn, 2004), PARFLOW-Surface Flow (Kollet and Maxwell, 2006), and PIHM (Qu and Duffy, 2007; Kumar, 2009). Among these, MIKE SHE, MODHMS, and PARFLOW-Surface Flow use finite difference methods, while InHM and WASH123D are based on finite element methods. Finite difference–based models have some significant advantages in terms of ease of meshing the domain, simple topological structure and ease of parallelization, but the rigidity of the structured grids in conforming to curvilinear geometries and representation of heterogeneities (Kumar et al., 2009) make it prohibitive to perform accurate large-scale simulations. Barrash and Dougherty (1997) and the USEPA (1994) also reported loss of accuracy in predicting hydraulic heads near regions of steep head gradients and boundaries using finite difference models. The inaccuracy can be reduced by performing relatively fine localized discretization in areas of steep head gradient (Leake and Claar, 1999; Mehl and Hill, 2004); however, this results in long execution times. An alternate solution strategy is the traditional Galerkin finite element methods, which are used to solve diffusion wave equations in WASH123D. These methods ensure continuity in gradient at the discretization boundary, but there is no local conservation of mass within each discretized unit element (Di Giammarco et al., 1996). Control volume finite element (CVFE) methods alleviate this problem (InHM is based on CVFE) and are able to conserve mass.

Here we develop a second-order accurate, fully coupled, finite volume–based integrated hydrologic modeling (FIHM) framework for unstructured grids. The primary advantages of this

M. Kumar and C.J. Duffy, Pennsylvania State Univ., 212 Sacket Bldg., University Park, PA 16802; K.M. Salvage, Geological Sciences and Environmental Studies, Binghamton State Univ., Binghamton, NY. *Corresponding author (muk139@psu.edu).

Vadose Zone J.
doi:10.2136/vzj2009.0014
Received 18 Feb. 2009.
Published online 13 Sept. 2009.

methodology are the conservation of the solution property within each discretized element, use of spatially adaptive and boundary-fitting unstructured mesh, which can be generated using boundary constraints pertaining to topography, hydrogeology, soils, or climate (Kumar et al., 2009), and numerical robustness achieved due to validity of local extremum diminishing property on each grid cell. The constrained unstructured mesh leads to enhanced efficiency in capture of topographic spatial variations with least number of elements, and also for the accurate capture of the complex geometries of topographic, geologic, and morphologic features. A higher-order scheme for overland flow (Fiedler and Ramirez, 2000; Lin et al., 2003) and subsurface flow (Manzini and Ferraris, 2004) yields improved simulation of states and derived hydraulic conductivity fields both in areas of smooth and steep gradients. The model simulates overland flow by solving the diffusion wave approximation of St. Venant's equation. Vadose zone pressure distribution is simulated by solving the nonlinear, three-dimensional Richards equation. The model treats the complete subsurface regime with unsaturated and saturated flow as a unified whole. The second-order accuracy of the scheme is achieved through the use of higher-order approximations of the flux at the cell faces (Turkel, 1985). We note that first-order finite volume models such as PIHM (Qu and Duffy, 2007; Kumar, 2009), which are based on a piecewise constant head representation within an element, lead to smearing of discontinuities and are particularly inaccurate for simulation in orthotropic and anisotropic media (Pasdunkorale and Turner, 2003). The second-order formulation in FIHM is supported by a continuously differentiable multidimensional slope limiter (developed by Jawahar and Kamath, 2000) to avoid spurious oscillations. The evaluation of local gradient at each edge of the control volume necessitates head magnitude at the cell centers and vertices. The model uses a pseudo-Laplacian–based reconstruction mechanism (Holmes and Connell, 1989) to obtain vertex head values from the cell averages (which are the primary unknowns). The reconstruction procedure is of fundamental importance to achieve optimally accurate normal flux at the edge (Bertolazzi and Manzini, 2004; Ollivier-Gooch and Van Altena, 2002). The model also handles modification of the flow field due to arbitrarily oriented anisotropy of hydrogeologic and physiographic properties. This is particularly important in regions with directional hydraulic conductivity or surface roughness. The majority of existing computational methods for anisotropic conductivity use structured, body-fitted meshes where, to avoid dealing with cross derivatives, they align their coordinate system with the principal directions of the conductivity tensor. Such a methodology is not easy to use in problems with multiple anisotropic materials. Even the finite volume–based models are generally not designed to handle both inhomogeneity and general anisotropy. The model detailed in this paper handles the media inhomogeneities in combination with full-tensor anisotropy by evaluating both the normal and tangential components of edge gradients.

The objectives of this paper are to detail the second-order accurate finite volume modeling framework for coupled surface and subsurface simulation and demonstrate its capability to simulate and improve understanding of process interactions. Specifically, we strive to understand why coupling of processes is needed and how the interaction between processes influences hydrologic states in the neighboring continua. Also, the influence of topographic and physiographic properties on process simulation will be explored. Complete details of testing and validation of the model are available in Kumar (2009). The six problems presented here highlight the model's capabilities and verify and explore individual processes and the interaction between them.

Governing Equations

The equations governing two-dimensional head distribution on the surface and a three-dimensional pressure distribution in the subsurface are presented in this section. Processes describing water movement on the surface and in the subsurface zone are discussed first, followed by coupling behavior between them.

Overland Flow

Overland flow is generally defined by the shallow-water St. Venant's equation. The equation is derived by depth-averaged integration of the three-dimensional Navier–Stokes equations. Application of a boundary condition on the free surface and continuity of flux on the ground surface during integration introduces a term that couples it to the vadose zone (Weiyan, 1992). Here we use a diffusion-wave flow–based approximation of St. Venant's equation with vadose zone–surface flow coupling terms as detailed in Gottardi and Venutelli (1993) by

$$\{\frac{\partial}{\partial x}[\psi_o K_x(\psi_o)\frac{\partial h_o}{\partial x}]+\frac{\partial}{\partial y}[\psi_o K_y(\psi_o)\frac{\partial h_o}{\partial y}]-Q_{og}\}+Q_{ss} = \frac{\partial \psi_o}{\partial t} \quad [1a]$$

or equivalently,

$$\{\nabla\cdot(\psi_o K(\psi_o)\nabla h_o)-Q_{og}\}+Q_{ss}=\frac{\partial \psi_o}{\partial t} \quad [1b]$$

where $K(\psi_o)$ is the diffusive conductance vector [L T^{-1}], ψ_o is the overland flow depth [L], h_o (= z_s + ψ_o) is the total overland flow head [L], z_s is the elevation of the ground surface [L], Q_{ss} is volumetric flux per unit area due to the sources or sinks, which can include precipitation and evapotranspiration [L T^{-1}], and Q_{og} is the vertical flux exchange per unit area between surface and subsurface flow [L T^{-1}]. The diffusive conductance term is given by

$$K(\psi_o)\big|_{x,y}=\frac{\psi_o^{2/3}}{n\big|_{x,y}}\frac{1}{\left(\left|\frac{dh_o}{ds}\right|\right)^{1/2}} \quad [2]$$

where n is Manning's roughness coefficient [$L^{-1/3}$ T] and s is the direction of maximum slope [L]. Note that the overland flow equation is a nonlinear parabolic equation due to the nature of the diffusive conductance. The assumptions inherent in the diffusion-wave approximation of St. Venant's equation include depth-averaged flow velocities, a hydrostatic vertical head distribution, mild bed slopes, neglecting inertial terms, and a dominant bottom shear stress. The equation is able to adequately resolve backwater effects.

Variably Saturated Subsurface Flow

Three-dimensional vadose zone flow in a heterogeneous porous medium is governed by Richards' equation for variably saturated flow (Huyakorn and Pinder, 1983) given by

$$\frac{\partial}{\partial x}[K_x(\psi)\frac{\partial h_g}{\partial x}]+\frac{\partial}{\partial y}[K_y(\psi)\frac{\partial h_g}{\partial y}] + \frac{\partial}{\partial z}[K_z(\psi)\frac{\partial h_g}{\partial z}]+Q_{ss}=[S.S_s+C(\psi)]\frac{\partial \psi}{\partial t} \quad [3a]$$

or equivalently,

$$\nabla\cdot(K(\psi)\nabla h_g)+Q_{ss}=[SS_s+C(\psi)]\frac{\partial \psi}{\partial t} \quad [3b]$$

where $K(\psi)$ is the hydraulic conductivity tensor [L T^{-1}], ψ is the potentiometric head [L], h_g (= z + ψ) is the total head [L], S is the soil saturation, S_s is the specific storage [L^{-1}], $C(\psi)$ is the specific moisture capacity [L^{-1}], and Q_{ss} is volumetric flux per unit volume [T^{-1}] due to the sources or sinks which can include pumping at wells. The [SS_s + $C(\psi)$] term in the variably saturated equation describes the storage properties of the medium. As the soil pressure head, ψ, becomes positive and the pores saturate with water, the specific moisture capacity, $C(\psi)$, converges to zero and the soil saturation, S, converges to one. The soil characteristic functions $K(\psi)$ and $C(\psi)$ can be represented by several different empirical and theoretical methods (e.g., Brooks and Corey, 1966; Mualem, 1976; Haverkamp et al., 1977; van Genuchten, 1980).

Coupling between Overland and Subsurface Flow

The coupling of the surface and vadose zone flow is incorporated by ensuring continuity of normal vertical flux and pressure head at the surface–subsurface interface. The methodology is equivalent to the "conductance concept" (VanderKwaak, 1999) if the thickness of the interficial domain goes to zero. Flux continuity across the surface–subsurface domain is ensured by equating Q_{og} in Eq. [1] to the vertical flux term $K_z(\partial h_g/\partial z)$ in Eq. [3], as discussed in Discacciati and Quarteroni (2002). The equivalent vertical conductivity, K_z, is evaluated as

$$K_z=\begin{cases} K_z(\psi) & \dfrac{\partial h_g}{\partial z}<0 \\ K_z(\psi=0) & \dfrac{\partial h_g}{\partial z}\geq 0 \end{cases} \quad [4]$$

We note that $\partial h_g/\partial z < 0$ corresponds to a negative downward gradient condition which essentially translates to flux in the upward direction (exfiltration). Also, continuity in head is ensured by setting

$$h_o\big|_{z=\text{surface}}=h_g\big|_{z=\text{surface}} \quad [5]$$

The physical equations defined on the problem domain are now defined on each discretized element (control volume) using a finite volume strategy.

Finite Volume Framework

Domain Discretization

The model FIHM uses a semidiscrete finite volume formulation to spatially discretize hydrologic process equations in the problem domain. The first step in doing so is the tessellation of the domain into a collection of nonoverlapping elements (control volumes) using an efficient domain discretization algorithm. We use constrained Delaunay triangulation to decompose the problem domain. In three dimensions, the triangulations are projected in depth to form prismatic elements. The Delaunay property of the grid leads to a large decrease in the number of nodes and elements with respect to structured meshes (Shewchuk 1996). Constraining of the Delaunay triangulations gives additional advantages through better representation of line features such as boundaries between zones having different soil types, or land-use or land-cover, rivers, and subwatershed divides (Kumar et al., 2009). The unique advantage of using thematic classes as constraints for unstructured grids is that all class boundaries (vegetation and/or soil polygons) are honored by the discretization, thus resulting in a model grid where every cell contains a single class. This reduces the data uncertainty arising from subgrid variability of mixed classes or themes within a model grid cell (Kumar et al., 2009). The discretization strategy generates high-quality unstructured grids with user-specified geometrical constraints such as element size and "roundness." The algorithmic details of generation of constrained Delaunay triangulations using geographical information system (GIS)–feature objects has been discussed in Kumar et al. (2009). More important, the discretization strategy has been integrated with a "shared data model," which leads to coupling of the GIS with the hydrologic model (Kumar, 2009). The integrated software framework facilitates rapid prototyping of meshes and data definitions resulting in efficient parameter steering, grid design, real-time visualization, and decision support. In summary, the "support-based" domain discretization and unstructured grid framework provides a close linkage between geoscientific data and FIHM (SoureForge, Mountain View, CA, http://sourceforge.net/projects/pihmgis/).

Semidiscrete Finite Volume Formulation

The governing partial differential equations (PDEs) describing surface and subsurface flow (Eq. [1] and [3]) are defined for each control volume using a semidiscrete finite volume formulation. The formulation entails discretization of a generalized PDE of a conservative scalar variable, ϕ, in space. We consider a generalized PDE (for surface or subsurface flow) as

$$\frac{\partial \varphi}{\partial t}=\nabla\cdot(\varphi U)+\nabla\cdot(\Gamma\nabla\varphi)+Q_{ss} \quad [6]$$

or the rate of change in ϕ = (advective flux) + (diffusive flux) + (source/sink), where U is the flux velocity vector, Γ is the conductivity tensor, and Q_{ss} is rate of increase/decrease in ϕ due to sources and sinks. The PDE in Eq. [6] is reduced to an ordinary differential equation (ODE) by integration over an arbitrary three-dimensional control volume, V_i, in the model domain

$$\int_{V_i}\frac{\partial \varphi}{\partial t}\mathrm{d}V = \int_{V_i}\nabla\cdot(\varphi U)\mathrm{d}V+\int_{V_i}\nabla\cdot(\Gamma\nabla\varphi)\mathrm{d}V+\int_{V_i}Q_{ss}\mathrm{d}V \quad [7]$$

By applying Gauss's theorem on the advective and diffusive terms on the right-hand side of the Eq. [7], we obtain

$$\frac{\partial}{\partial t}\int_{V_i}\varphi \mathrm{d}V = \int_{A_{ij}}\vec{n}\cdot(\varphi U)\mathrm{d}A + \int_{A_{ij}}\vec{n}\cdot(\Gamma\nabla\varphi)\mathrm{d}A + \int_{V_i}Q_{ss}\mathrm{d}V \quad [8]$$

where $\vec{n}$ is the normal vector to the surface j of the control volume i. By integrating the individual flux terms in Eq. [8] over a prismatic volume, we obtain a generic semidiscrete form of ODE that defines all the hydrologic processes incorporated in the finite volume as

$$A_i\frac{\mathrm{d}\bar{\phi}}{\mathrm{d}t} = \sum_j \vec{n}\cdot\vec{C}A_{ij} + \sum_j \vec{n}\cdot\vec{D}A_{ij} + \bar{Q}_{ss}V_i \quad [9]$$

where $\bar{\phi}$ (L) is the average volumetric conservative scalar per unit planimetric prismatic volume area A_i, A_{ij} is the interfacial area, $\vec{C}$ and $\vec{D}$ are the advective and diffusive flux, respectively, $\vec{n}$ is normal vector to the face of control volume and $\bar{Q}_{ss}$ is the average source–sink rate per unit control volume. We use this approach to convert the governing PDEs for surface (Eq. [1]) and subsurface (Eq. [3]) flows to their semidiscrete form of ODEs. As discussed in the previous section, both governing equations are parabolic diffusion–based PDEs, so the convective flux $\vec{C}$ in Eq. [9] will be equal to zero. We can express the semidiscrete forms of [1] and [3] as

$$A_i\frac{\mathrm{d}\psi_o}{\mathrm{d}t} = \sum_{j=1}^{3}\vec{n}_j\cdot\vec{F}_j + \sum_{k=1}^{2}\vec{n}_k\cdot\vec{G}_k + Q_{ss}V_i \quad [10]$$

$$\left\{A_i[S\cdot S_s + C(\psi)]\frac{\mathrm{d}\psi}{\mathrm{d}t} = \sum_{j=1}^{3}\vec{n}_j\cdot\vec{F}_j + \sum_{k=1}^{2}\vec{n}_k\cdot\vec{G}_k + Q_{ss}V_i\right\}\Big|_m \quad [11]$$

where $\vec{F}_j$ and $\vec{G}_k$ are lateral and vertical flux vectors. j and k denote the faces of the ith control volume element and m is the vertical discretization index. Note that since the control volumes are prismatic in shape, there are a total of five faces (edges): three vertical faces on the side of the prism and two horizontal faces on the top and bottom of the prism.

Vertical Flux Calculation

The vertical subsurface flux term $\vec{G}_k$ at the interface between mth and $(m + 1)$th layer (see Fig. 1) is calculated by imposing continuity of flux and head at the interface and is given by

$$\vec{G}_k = K(\psi)\big|_{m,m+1}A_i\nabla h \quad [12a]$$

We note that continuity in flux requires

$$\vec{G}_k\big|_{m,m+1} = \vec{G}_k\big|_{m,m+1/2} = \vec{G}_k\big|_{m+1/2,m+1} \quad [12b]$$

or

$$K(\psi)\big|_m A_i\left[\frac{(h)_m - (h)_{m+1/2}}{0.5\Delta z_m}\right] = K(\psi)\big|_{m+1}A_i\left[\frac{(h)_{m+1/2} - (h)_{m+1}}{0.5\Delta z_{m+1}}\right]$$

This results in calculation of the vertical flux as

$$\vec{G}_k\big|_{m,m+1} = \frac{2K(\psi)\big|_{m+1}K(\psi)\big|_m}{K(\psi)\big|_{m+1}\Delta z_m + K(\psi)\big|_m\Delta z_{m+1}}A_i\left[(h)_m - (h)_{m+1}\right] \quad [13]$$

Both the flux and the vertical anisotropy along the z-axis have been assumed to be normal to the control volume face in this analysis. The flow between surface and subsurface domains follows similar conceptualization. The flux at the topmost face of the subsurface prismatic volume ($\vec{G}_k$ in Eq. [11]) is equal to the bottom flux from the overland-flow control volume ($\vec{G}_k$ in Eq. [10], which is the same as Q_{og} in Eq. [1]). The coupling flux $\vec{G}_k$ in this case can be calculated as

$$\vec{G}_k\big|_{0,1} = \vec{G}_k\big|_{0,1/2} = \vec{G}_k\big|_{1/2,1} \quad (\text{continuity in flux}) \quad [14a]$$

By ensuring continuity in head at the land surface ($h_0 = h_{1/2}$) and evaluating the effective vertical conductivity as in Eq. [4], reduces the above equation to

$$\vec{G}_k\big|_{0,1} = K_z A_i\left[\frac{(h)_0 - (h)_1}{0.5\Delta z_1}\right] \quad [14b]$$

Note that $(h)_0$ and $(h)_1$ in the above equation are h_o and h_g in Eq. [1] and [3], respectively.

Lateral Flux Calculation

The normalized lateral flux term ($\vec{n}_j\bullet\vec{F}_j$) for surface flow in Eq. [10] is derived as

$$\vec{n}_j\cdot\vec{F}_j = \int_{A_{ij}}\vec{n}\cdot(K(\psi_o)\nabla h_o)\mathrm{d}A = \int_{\xi_{ij}}\vec{n}\cdot[\psi_o K(\psi_o)\nabla h_o]\mathrm{d}\xi = UW[\psi_o K(\psi_o)\nabla h_o]\big|_{\xi_{ij}}\cdot\xi_{ij} \quad [15a]$$

and for the subsurface flux in Eq. [11] is derived as

$$\vec{n}_j\cdot\vec{F}_j = \int_{A_{ij}}\vec{n}\cdot\left[K(\psi)\nabla h_g\right]\mathrm{d}A = \int_{\xi_{ij}}\vec{n}\cdot\left[\Delta z K(\psi)\nabla h_g\right]\mathrm{d}\xi = UW[\Delta z K(\psi)\nabla h_g]\big|_{\xi_{ij}}\cdot\xi_{ij} \quad [15b]$$

where ξ_{ij} is edge length of the jth edge (or face) of element i, ψ_o is the overland flow depth, and Δz is the vertical discretization

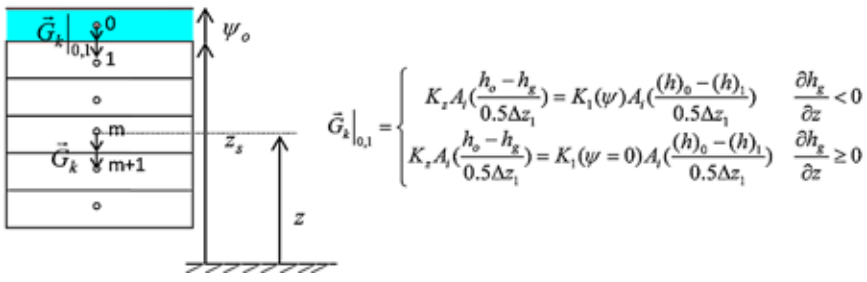

FIG. 1. Each prismatic element is discretized in vertical into multiple layers. Δz_{m+1} is thickness of $(m + 1)$th discretization layer. Layer 0 (shaded) corresponds to overland flow depth, ψ_0. G_k is the vertical flux at the interface of the mth and $(m + 1)$th layers; h_o [= $(h)_0$] and h_g [= $(h)_1$] are the heads of the overland flow and in the top subsurface layer respectively; z_s is the elevation to the ground surface; and A_i is the planimetric area of the prismatic element.

thickness of a given subsurface control volume. *UW*[ ] is an upwind function that determines the cell face at which normalized flux for the edge is calculated. The cell face identified belongs to the upstream cell from which flow is directed outwards through the edge. The line integrals in Eq. [15] are computed by applying second-order midpoint quadrature rule to upstream numerical fluxes (Blazek, 2001). The calculation of lateral flow terms for both surface and subsurface flow (in Eq. [15]) crucially depends on the evaluation of gradient and head terms on the edge faces of each control volume. In the following discussion, h corresponds to total head of either subsurface head or overland flow head.

Edge Gradient Calculation

The first step in the formulation of the discrete gradient for internal or boundary edges consist of defining the one-sided gradient. The gradient calculation for the variational triangle $\Delta a1b$ (shown in Fig. 2) for the edge ab is calculated using the Green–Gauss theorem as

$$\nabla h = \frac{1}{A}\oint_{\xi} \vec{n}\cdot h \mathrm{d}\xi \qquad [16]$$

where ξ is the edge vector and A is the area of the $\Delta a1b$. Along the x and y directions, the gradient reduces to

$$(\nabla h)_{a1b}\big|_x = -\frac{y_a(h_b-h_1)+y_1(h_a-h_b)+y_b(h_1-h_a)}{x_a(y_b-y_1)+x_1(y_a-y_b)+x_b(y_1-y_a)} \qquad [17a]$$

$$(\nabla h)_{a1b}\big|_y = -\frac{x_a(h_b-h_1)+x_1(h_a-h_b)+x_b(h_1-h_a)}{y_a(x_b-x_1)+y_1(x_a-x_b)+y_b(x_1-x_a)} \qquad [17b]$$

The absolute gradient for the left variational triangle of edge ab is given by

$$\nabla h\big|_L = (\nabla h)_{a1b} = \sqrt{\left[(\nabla h)_{a1b}\big|_x\right]^2 + \left[(\nabla h)_{a1b}\big|_y\right]^2} \qquad [18]$$

We note that the gradient calculation in Eq. [17] and [18] depends both on the cell center heads (such as h_1) and the vertex heads (such as h_a and h_b). We use a multidimensional linear (second-order) reconstruction scheme within the framework of cell-centered finite-volume discretization to determine vertex values from cell averages.

Vertex Reconstruction

A second-order accurate, modified pseudo-Laplacian procedure (Jawahar and Kamath, 2000) is used to obtain vertex values from the corresponding cell-centered values (Holmes and Connell, 1989). The method outperforms the traditionally used inverse-distance weighted interpolation, which was observed to have less-than-second-order accuracy (Frink, 1994). For any vertex of the mesh, we first define the reconstruction stencil as the union of the cells that share the vertex; then, we calculate a cell weight for every element of the stencil. Figure 3 shows a representative stencil for the vertex b. The value of head at vertex b is calculated as

$$h_b = \sum_{i=1}^{M} \frac{\omega_i}{\sum_{i=1}^{M}\omega_i} h_i \qquad [19]$$

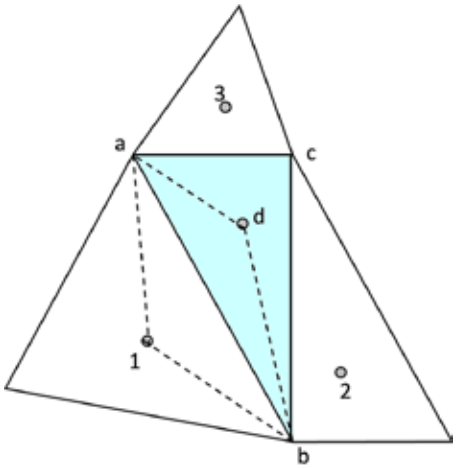

FIG. 2. Plan view of a typical tessellation where Δabc is surrounded by three neighboring elements (having centers 1, 2, and 3). Flux calculation on any edge ab of Δabc (shaded) uses heads at vertices a and b of the triangle and at cell centers 1 and d.

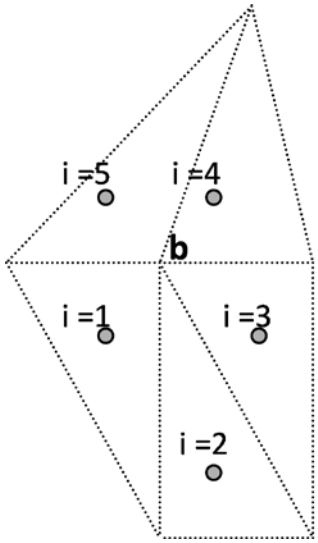

FIG. 3. Head reconstruction at an arbitrary vertex b in a tessellation using a pseudo-Laplacian procedure (Jawahar and Kamath, 2000) uses head values at the centers of all the cells that share a node at b.

where M is the number of cells sharing the vertex and ω_is are the cell weights that are made to satisfy the zero pseudo-Laplacian condition (Kim et al., 2003). The weighted interpolation formula is linearly consistent. The individual weights are calculated by using Lagrange multipliers λ_x and λ_y as

$$\omega_i = 1+\lambda_x(x_i-x_b)+\lambda_y(y_i-y_b) \qquad [20]$$

where

$$\lambda_x = \frac{I_{xy}R_y - I_{yy}R_x}{I_{xx}I_{yy}-I_{xy}^2} \quad \lambda_y = \frac{I_{xy}R_x - I_{xx}R_y}{I_{xx}I_{yy}-I_{xy}^2} \qquad [21a]$$

$$I_{xx} = \sum_{i=1}^{M}(x_i-x_b)^2 \quad I_{yy} = \sum_{i=1}^{M}(y_i-y_b)^2$$
$$I_{xy} = \sum_{i=1}^{M}(x_i-x_b)(y_i-y_b) \qquad [21b]$$

$$R_x = \sum_{i=1}^{M}(x_i - x_b) \quad R_y = \sum_{i=1}^{M}(y_i - y_b) \qquad [21c]$$

This procedure gives most of the benefits of a true Laplacian and is also computationally inexpensive. It is important to realize that this reconstruction step is required by all vertices of the mesh, whether the vertex is internal or on the boundary of the computational domain. Extraneous cell weights (negative or positive values that are greater than 2), which are sometimes obtained at the boundaries (Frink and Pirzadeh, 1999), are clipped based on Jawahar and Kamath (2000). The modification of weights, which is only performed for the boundary vertices, is not expected to have a significant impact on accuracy since subsequent imposition of boundary conditions at these locations would weaken the effect.

Calculation of Head at an Edge Using Linear Reconstruction

The overland flow depth value at an edge in Eq. [15a] can be approximated by either using an upwind cell-centered value (characteristic of first order methods) or obtaining an interpolated value at the midpoint of the edge. First-order upwind methods introduce large and often unacceptable numerical diffusion. Here we use a second-order estimate of the solution at the edge by approximating the edge depth using a multidimensional linear reconstruction process. The underlying assumption is a piecewise linear distribution of flow depth within a cell. To satisfy C-property (Bermudez and Vasquez, 1994), instead of linear distribution of flow depth, we perform interpolation of the total head at the edge and then subtract the elevation at the edge to obtain flow depth at the edge. The higher-order edge estimate, h_ξ, is calculated by

$$h_\xi = h_c + \vec{r} \cdot \nabla h_l \qquad [22]$$

where h_c is the head at the cell center, $\vec{r}$ is the position vector of the midpoint of the edge face with respect to the cell center, and ∇h_l is the limited cell gradient. This reconstruction technique is based on a wide computational stencil and does not strongly depend on vertex values to preserve stability for highly distorted grids.

Limited Gradient Calculation

The linear reconstruction can cause spurious numerical oscillations when approximating strong gradient solutions. The problem is alleviated by a limiter-based gradient calculation that locally monotonizes the reconstructed solution by limiting the slope of the reconstructed variables. The limiter helps in achieving smooth transition for both discontinuous jumps and continuous gradients. Here we use a multidimensional limiter of Jawahar and Kamath (2000) that is shown to be effective for strong discontinuities, even on a grid composed of highly distorted triangles. This is in contrast to the often-used nondifferentiable extremum seeking limiters such as the ones based on the MUSCL approach (Hubbard, 1999), which are strongly dependent on grid connectivity. The limiting procedure consists of calculation of limited gradient (∇h_l) by taking the weighted average of the unlimited gradients (∇h_u) in the neighboring elements as

$$\nabla h_l = \omega_1(\nabla h_u)_1 + \omega_2(\nabla h_u)_2 + \omega_3(\nabla h_u)_3 \qquad [23]$$

where the weights are

$$\omega_1 = \frac{g_2 g_3 + \varepsilon^2}{g_1^2 + g_2^2 + g_3^2 + 3\varepsilon^2} \quad \omega_2 = \frac{g_3 g_1 + \varepsilon^2}{g_1^2 + g_2^2 + g_3^2 + 3\varepsilon^2}$$
$$\omega_3 = \frac{g_1 g_2 + \varepsilon^2}{g_1^2 + g_2^2 + g_3^2 + 3\varepsilon^2} \qquad [24]$$

and g_1, g_2, and g_3 are the square of the L_2 norm of the unlimited elemental gradients given by $g_1 = \|(\nabla h_u)_1\|^2$, $g_2 = \|(\nabla h_u)_2\|^2$, and $g_3 = \|(\nabla h_u)_3\|^2$; ε is a small number introduced to prevent indeterminacy. The limiting weights in Eq. [23] are reduced to 1/3 when all the three elemental gradients are equal.

Unlimited Gradient Calculation

The unlimited gradient of an element, ∇h_u, is the area weighted average of gradients calculated on its edges, ∇h_e. This implies that

$$\nabla h_u = \sum_{i=1}^{3}(A_e)_i(\nabla h_e)_i \qquad [25]$$

where $(A_e)_i$ is the cumulative area of the variational triangle on the either side of edge *i*. Using Fig. 2, the edge gradient on an arbitrary face *ab* can be calculated as

$$(\nabla h_e)_{ab} = \frac{A_{ab1}\nabla h_{ab1} + A_{abd}\nabla h_{abd}}{A_{ab1} + A_{abd}} \qquad [26]$$

In the above equation, $(A_e)_{ab} = A_{ab1} + A_{abd}$. For faces located on the boundaries, the solution at ghost elements is used to provide the same stencil to compute the face gradients.

Normalized Lateral Flux in Heterogeneous Anisotropic Domain

Evaluation of normalized flux at an edge must take into account the contribution of arbitrarily oriented anisotropy at the control volume interface. The normalized flux $\vec{n}_j \cdot \vec{F}_j$ in a two-dimensional anisotropic domain with principal axes oriented as shown in Fig. 4 can be resolved into *x* and *y* components according to Bear (1975) as

$$\vec{n} \cdot \vec{F} = \vec{n} \cdot (F_x \hat{i} + F_y \hat{j}) = \vec{n} \cdot (K_x \nabla h_x \hat{i} + K_y \nabla h_y \hat{j}) A_\xi \qquad [27]$$

where ∇h_x and ∇h_y are calculated as in Eq. [17], and K_x and K_y are hydraulic conductivity components in the *x* and *y* directions, respectively; A_ξ is the edge interaction–flux area, which is equal to $\psi_o \xi$ for surface flow and $\Delta z \xi$ for vadose zone. Assuming that principal conductivities K_1 and K_2 are oriented at an angle β to the global *x*–*y* axes (see Fig. 4), Eq. [27] becomes

$$\vec{n} \cdot \vec{F} =$$
$$A_\xi \left\{ \left[(K_1 \mathrm{Cos}^2\beta + K_2 \mathrm{Sin}^2\beta)\nabla h_x + (K_1 - K_2)\mathrm{Cos}\beta * \mathrm{Sin}\beta \nabla h_y \right] \hat{i} \right.$$
$$\left. + \left[(K_1 - K_2)\mathrm{Cos}\beta * \mathrm{Sin}\beta \nabla h_x + (K_1 \mathrm{Sin}^2\beta + K_2 \mathrm{Cos}^2\beta)\nabla h_y \right) \hat{j} \right\} \cdot \vec{n} \qquad [28]$$

The conductivities in the above equation can be either a diffusive conductivity shown in Eq. [2] for the surface flow or a hydraulic conductivity of the subsurface domain. Taking into account the

orientation of normalized flux that is at an angle α to the global *x*-axis (see Fig. 4), Eq. [28] can be rewritten as

$$\vec{n}\cdot\vec{F} = A_\xi\left[(K_1\mathrm{Cos}^2\beta + K_2\mathrm{Sin}^2\beta)\nabla h_x + (K_1 - K_2)\mathrm{Cos}\beta * \mathrm{Sin}\beta\nabla h_y\right]\mathrm{Cos}\alpha + \left[(K_1 - K_2)\mathrm{Cos}\beta * \mathrm{Sin}\beta\nabla h_x + (K_1\mathrm{Sin}^2\beta + K_2\mathrm{Cos}^2\beta)\nabla h_y\right]\mathrm{Sin}\alpha \quad [29]$$

By replacing $\nabla h_x = \nabla h\mathrm{Cos}\theta$ and $\nabla h_y = \nabla h\mathrm{Sin}\theta$ in Eq. [29], the equation transforms to

$$\vec{n}\cdot\vec{F} = A_\xi\left[K_1\mathrm{Cos}(\theta-\beta)\mathrm{Cos}(\alpha-\beta) + K_2\mathrm{Sin}(\theta-\beta)\mathrm{Sin}(\alpha-\beta)\right]\nabla h \quad [30]$$

where θ is angle of orientation of ∇h to the *x*-axis. An alternative derivation of Eq. [30] using a coordinate system that is oriented along the direction of principal conductivities is given in the Appendix.

Implicit Time Integration

The semidiscrete scheme shown in Eq. [10] and [11] forms a system of differential equations, which can be written as

$$\frac{\mathrm{d}\psi}{\mathrm{d}t} = f\left[t, \psi(t)\right] \quad [31]$$

where the vector $\psi(t)$ is defined by

$$\psi(t) = [\psi(x_{1,1}, y_{1,1}, z_{1,1}, t), \ldots, \psi(x_{N,1}, y_{N,1}, z_{N,1}, t), \psi(x_{1,2}, y_{1,2}, z_{1,2}, t), \ldots, \psi(x_{N,M}, y_{N,M}, z_{N,M}, t)]$$

where *M* is the number of states, which includes overland flow and variably saturated heads in vertically discretized subsurface layers, *N* is the number of lateral discretization elements, and ($x_{i,j}$, $y_{i,j}$, $z_{i,j}$) is the coordinate location of centroid of the *i*th cell and *j*th layer. For time integration, we use a variable-order, variable-step backward differentiation formula–based stiff ODE solver called CVODE (Cohen and Hindmarsh, 1994). Using Newton linearization scheme, CVODE solves the system given in Eq. [31], at each time step, by reducing it to

$$A[\psi^{n(k+1)} - \psi^{n(k)}] = -G(\psi^{n(m)}) \quad [32]$$

where

$$A = I - T_n\beta_{n,0}J \quad [33]$$

and where $\psi^{n(k)}$ in Eq. [32] are computed approximations to $\psi(t_n)$ at iteration *k*; $T_n = t_n - t_{n-1}$ is the step size; *I* is the identity matrix, *J* is the Jacobian, and β is a coefficient that is uniquely determined by the order and recent history of the step sizes (Byrne and Hindmarsh, 1975; Jackson and Sacks-Davis, 1980). Preconditioned, iterative Krylov method is used to solve the Jacobian system at each Newton iteration step (Brown and Hindmarsh, 1989). The advantage of doing so using Krylov linear solver is that it requires only matrix vector products, which can be approximated by taking differences of the nonlinear function *f*( ). This approach avoids computation and storage of the Jacobian matrix. The memory efficiency, however, is obtained at the expense of increased computational time arising from additional evaluation of the nonlinear function. The function *G*( ) in the Eq. [32] is the nonlinear system given by

$$G(\psi^n) = \psi^n - T_n\beta_{n,0}f(t_n, \psi_n) - \sum_{i=1}^{Q}\alpha_{n,i}\psi^{n-i} \quad [34]$$

where *Q* is the accuracy order that varies from 1 to 5, and α is a coefficient uniquely determined by the order and recent history of the step sizes (Byrne and Hindmarsh, 1975; Jackson and Sacks-Davis, 1980). At each iteration step in Eq. [32], the local error is estimated and is required to satisfy convergence tolerance conditions. The time step size taken during iteration is reduced whenever that error test fails. In addition to adjusting the step size to meet the local error test, CVODE also adjusts the order, with the goal of maximizing the step size. The integration starts out at order 1 and the order varies dynamically after that. However, if either a convergence failure or an error test failure occurred on the step just completed, no change in step size or order is performed (Cohen and Hindmarsh, 1994). By varying the step size and order, the solver aims for the most efficient simulation while ensuring stability.

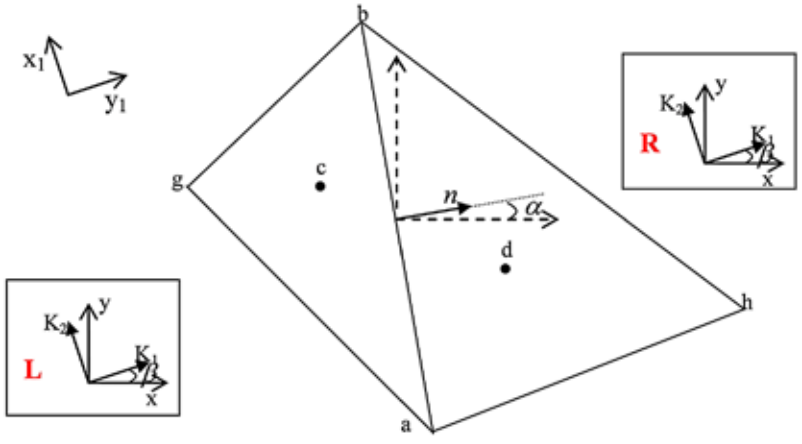

FIG. 4. Arbitrarily oriented anisotropy in adjacent cells sharing interface *ab*. Note that principal conductivities (K_1, K_2) and their orientation (angle β) with respect to the global Cartesian coordinate system (*x*,*y*) for both left (L) and right (R) cells can be different. (x_1,y_1) is a local coordinate system that is oriented along the directions of the principal axes of anisotropy. The vector normal to interface *ab, n,* is at an angle α to the global *x* axis.

Numerical Results

To illustrate the effectiveness of the developed modeling framework, six test case problems are presented in this section. Complete testing and validation of the model, using additional test cases, were detailed in Kumar (2009). The model simulations were performed on dual 2.4 GHz AMD Opteron processors with 8 Gb of ECC RAM.

Infiltration through Layered Soil

An unsaturated vertical flow experiment in a two-layered soil was used to verify flow behavior in unsaturated zone. We compare the simulation result with analytical solutions obtained by Srivastava and Yeh (1991). Exponential functional forms were used to denote the saturation pressure-head relations and conductivity curves in both the layers as shown in Eq. [35]:

$$K(\psi) = K_s e^{\alpha\psi} \text{ and } S = \frac{\theta - \theta_r}{\theta_s - \theta_r} = e^{\alpha\psi} \quad [35]$$

where K_s is saturated hydraulic conductivity, θ is the moisture content, and α is a soil pore size distribution parameter. The α of the two layers is set to be equal to 0.1 cm^{-1}, and K_s for the lower and upper layers are equal to 1 and 10 cm h^{-1}, respectively; the thickness of each layer is 100 cm; and θ_r and θ_s (residual and saturated moisture contents, respectively) are taken as 0.06 and 0.4, respectively. The domain is discretized into 200 prismatic layers of 1-cm thickness each. Initial pressure distribution in the two layers corresponds to the steady-state infiltration profile when a constant flux is applied at the soil surface and a prescribed pressure is maintained at the lower boundary. Solutions are obtained for wetting and drying cases to test the robustness of the model. During wetting scenario, the infiltration rate (constant flux at the top of soil column), initially equal to 0.1 cm h^{-1}, is suddenly increased to 0.9 cm h^{-1} at the start of simulation, while for the drainage scenario, it is decreased from an initial value of 0.9 cm h^{-1} to 0.1 cm h^{-1}. Figure 5 shows calculated pressure head distributions at selected times during the infiltration event as computed with the analytical equation derived in Srivastava and Yeh (1991) and the numerical model presented in this paper. In both cases, infiltration starts in the upper, high conductivity layer. Once the wetting front reaches the top of the less-conductive layer, the pressure head at the interface increases rapidly to translate the flux and maintain mass balance. An excellent match between numerical and analytical models is observed. The computation time needed to perform simulation for either case was less than 1 s.

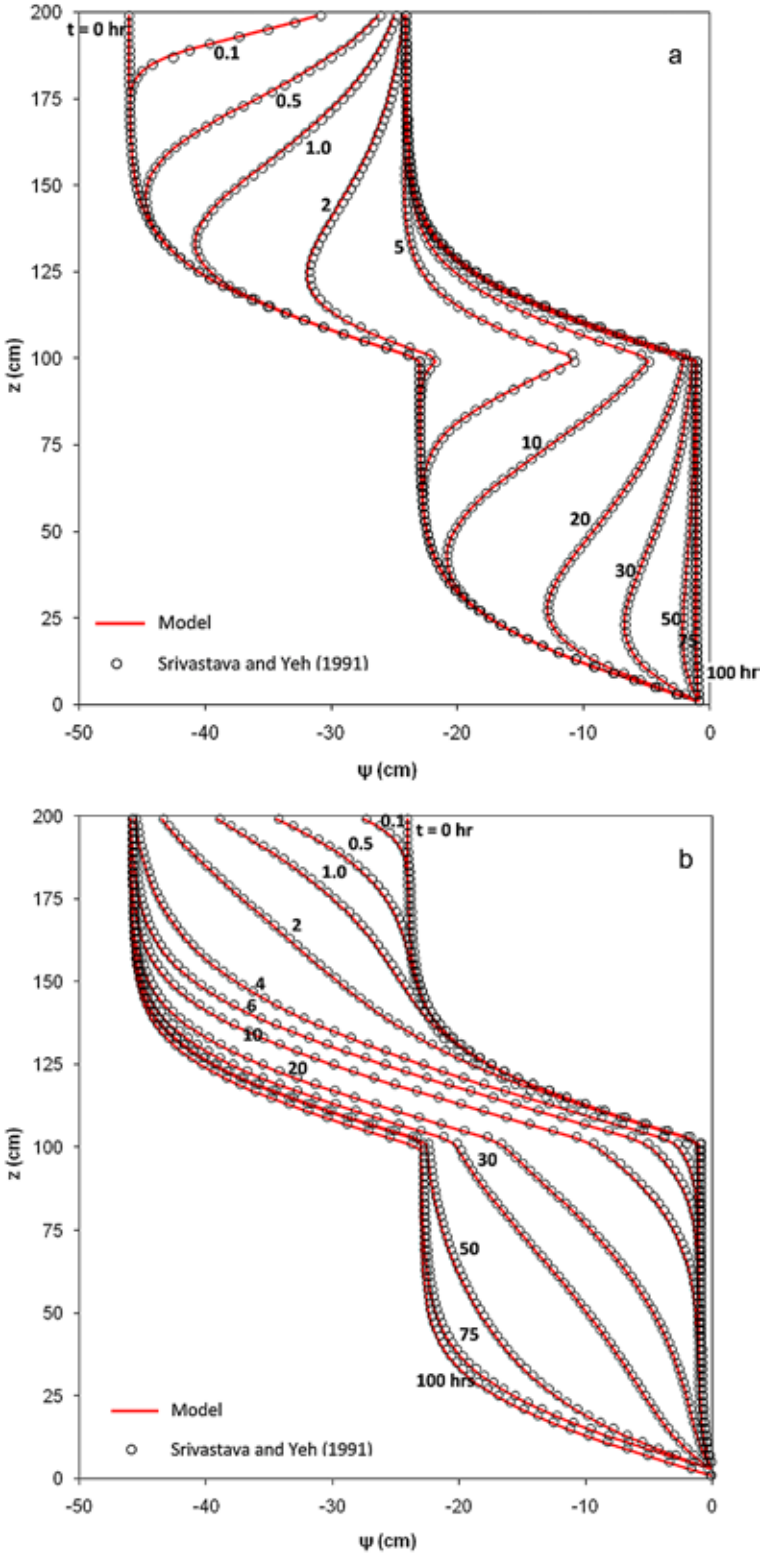

FIG. 5. (a) Wetting behavior in a layered soil during the infiltration experiment based on Srivastava and Yeh (1991). (b) Drying behavior in a layered soil during the infiltration experiment based on Srivastava and Yeh (1991). ψ is the potentiometric head, and z is elevation of the soil layer above ground water table (lower boundary condition).

Pumping in Three-Dimensional Homogeneous Orthotropic Domain

Verification of the three-dimensional variably saturated component in the numerical model was performed by comparing pumping test results in an artificial, asymmetric, and orthotropic domain to results obtained by 3DFEMWATER (Yeh and Cheng, 1994). The domain is cuboidal in shape with dimensions of 72 m (in z) by 800 m (in y) by 1000 m (in x), as shown in Fig. 6. The pumping well is located at (x, y) = (540, 400 m). Initially, the whole domain is in hydrostatic equilibrium with total head being 60 m everywhere. The top, bottom, front, and rear extremes of the domain are no-flow boundaries, while the head on the left and right boundaries is held constant at 60 m. For the time of simulation, the head at the well is lowered and maintained at a height of 30 m. As a result, the water table profile changes continuously until the system reaches steady state. The soil is anisotropic with saturated hydraulic conductivity components in x, y, and z directions being equal to 5, 0.5, and 2 m d^{-1}, respectively. The porosity, θ_s, and residual moisture capacity, θ_r, of the medium are equal to 0.25 and 0.0125, respectively. The moisture content, unsaturated conductivity and head are related through a variant of the van Genuchten equation as shown in Eq. [36]:

$$\theta = \theta_r + \frac{\theta_s - \theta_r}{1 + (\alpha|\psi_a - \psi|)^{\beta}} \quad K_r = \left(\frac{\theta - \theta_r}{\theta_s - \theta_r}\right)^2 \quad [36]$$

where ψ_a is air entry pressure, and β and α are potentiometric parameters. The values of ψ_a, β, and α are 0, 0.5, and 2.0, respectively. The specific storage was assumed to be zero. The model domain was discretized into 2597 elements horizontally and 26 layers vertically. The top 21 layers were of 2 m thickness, while the remaining five were of 6 m thickness each. This dichotomy in discretization coincided with the height of well head (30 m from the bottom). The steady-state solution was also obtained for a horizontally isotropic case by considering conductivity along the *y* axis to be equal that along the *x* axis, 5 m d^{-1}. Modeled water table elevations were compared with the results obtained from 3DFEMWATER (Yeh and Cheng, 1994) along a cross-section in the *x*–*z* plane passing through the center of the well. An excellent match between the two results is observed and is shown in Fig. 7. The model was run for a period of 300 d before it reached steady state. The simulation time for the experiment was 1491 s. In the second case, the larger hydraulic conductivity in the *y*-direction impacts the cone of depression that develops in the *x*-direction as well, with less drawdown occurring at a given location. This experiment verifies the conceptualization of three-dimensional variably saturated flow in presence of constant head (at the well and at the left and right extremes) and no-flux (at the top and bottom extremes) boundary condition in an orthotropic media. We further explore the effect of anisotropy on variably saturated flow (i) when principal directions of anisotropy are not aligned with model domain orientation and (ii) in a heterogeneous, anisotropic domain in the next two sections.

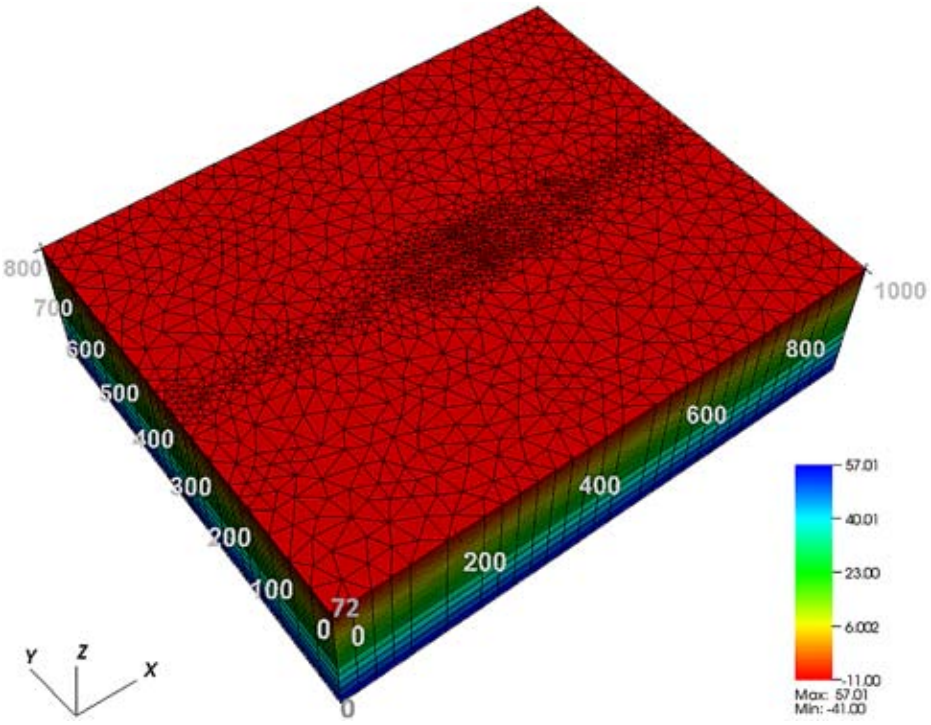

FIG. 6. Initial head distribution for a three-dimensional well pumping experiment in an orthotropic media. The well is located at (*x*, *y*) = (540, 400 m). The domain is discretized into 67,522 prismatic elements. Finer discretization along the *x*–*z* plane passing through the well was utilized to compare the results with existing solutions.

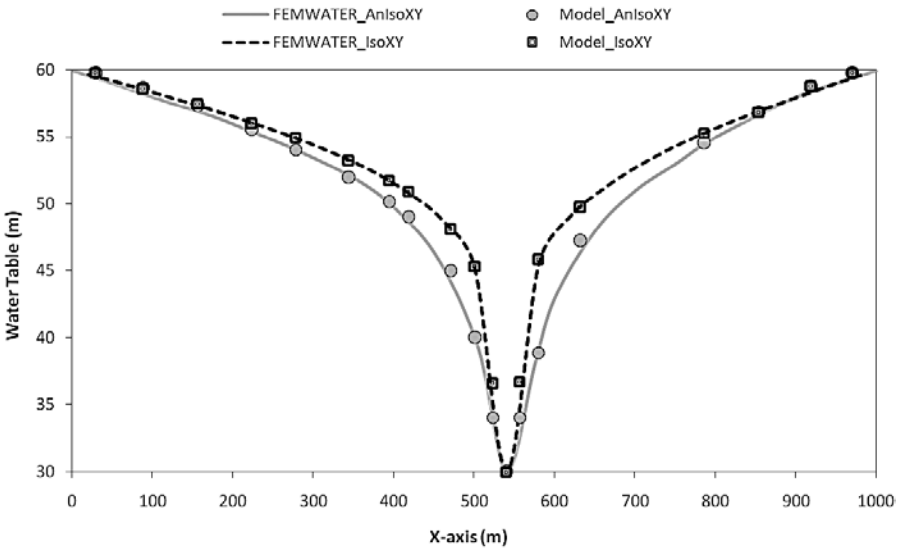

FIG. 7. Water table drawdown at steady state in the orthotropic media that was shown in Fig. 6. The FIHM model results have been compared to base results from FEMWATER for horizontal anisotropic (FEMWATER_AnIsoXY and Model_AnIsoXY) and isotropic (FEMWATER_IsoXY and Model_IsoXY) cases.

Flow Modification due to Phase Shifted Anisotropy

In an anisotropic domain with principal axes direction not being coincident with the direction of maximal gradient, the resultant flux vector gets oriented in a new direction. Additionally, if the model grid coordinates are not oriented in the principal axes direction, numerical simulation for the flux necessitates proper resolution of each flux component due to anisotropy. Flow modification due to the phase shift is explored further using a setup very similar to the one explained in the previous section. The properties of the model domain in this experiment are the same as those in the previous section unless specified otherwise. For computational efficiency, the aquifer's thickness was reduced to 2 m (in *z*), and vertical discretization was limited to one layer. The initial head in the model domain is set to 0 m. A reduced head of –30 m is maintained at the well location during the simulation. Two numerical experiments were conducted to observe the relative change in flow behavior. In the first experiment, the principal directions of saturated anisotropic conductivity (equal to 20 m d^{-1} and 0.5 m d^{-1} in horizontal and 2 m d^{-1} in vertical) are oriented along the grid coordinates. The second

experiment has principal directions of horizontal conductivity oriented at a 30-degree angle to the model coordinates. The results of both simulations are shown in Fig. 8. Computational time was 868 s. Due to the acute anisotropy, the potentiometric drawdown contours are elliptical and their major axis is oriented along the principal direction of anisotropy. Several other models

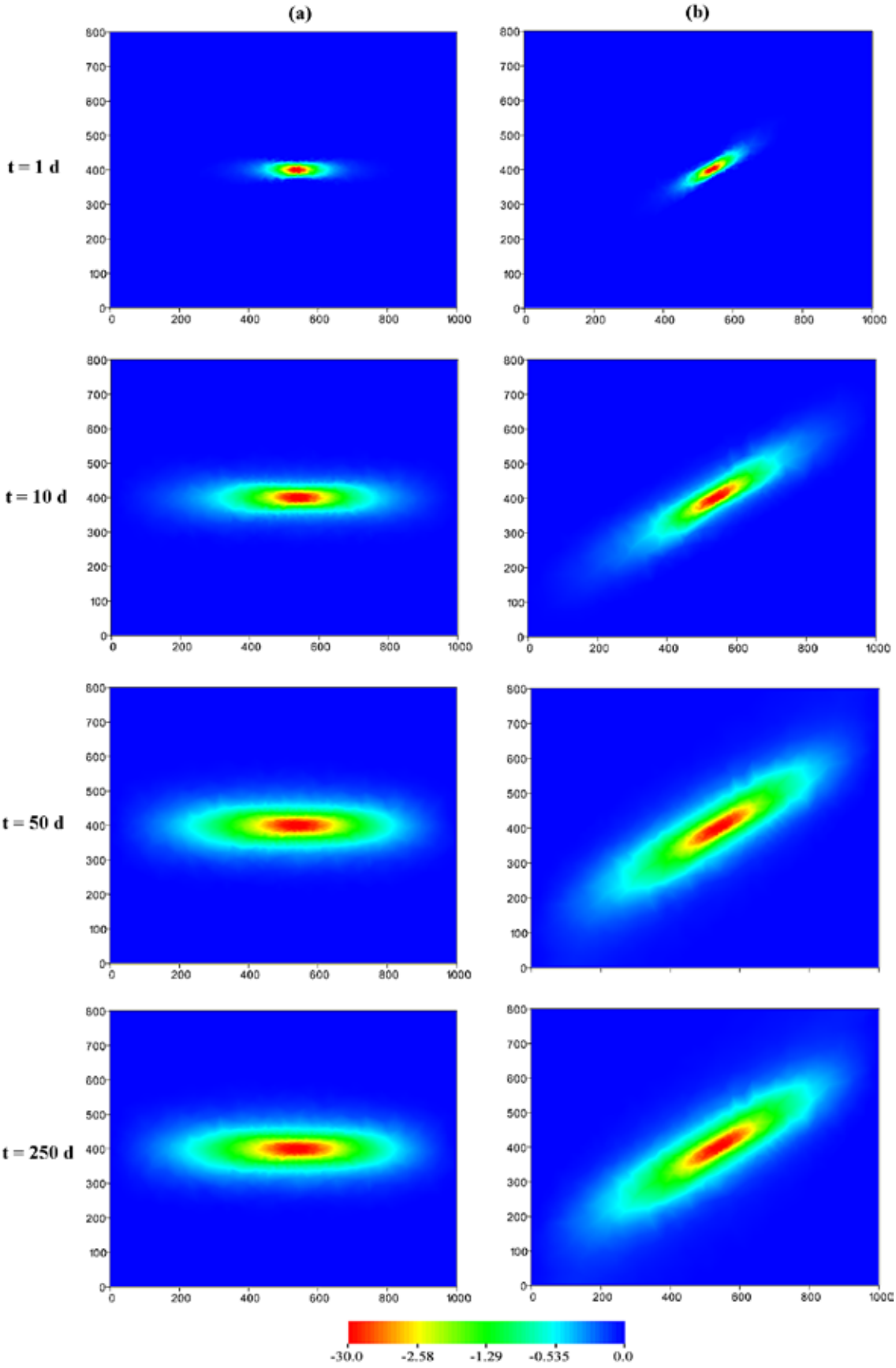

FIG. 8. Transient well drawdown in an anisotropic domain with principal axis of conductivity (a) oriented along the direction (*x*–*y*) of gradient due to specified head on left and right boundaries (equal to 60 and 30 m, respectively), and (b) oriented at 30-degree angle to gradient direction. Note the rotation of the cone of depression along the principal direction of conductivity in case (b). *t* = time.

(such as MODFLOW and ModHMS) are also able to simulate anisotropic flow in a homogeneous domain by avoiding cross-derivative terms through alignment of the model coordinate system along the direction of anisotropy. FIHM is unique in terms of its flexibility to simulate flow behavior in heterogeneous, anisotropic domain with multiple anisotropic zones. This is achieved by (i) constrained domain discretization of the heterogeneous domain such that each elemental volume is assigned a unique property only; the constrained unstructured meshes also preserve the boundaries accurately; and (ii) a generic formulation of anisotropic flux on arbitrarily oriented control volume faces. A representative simulation in heterogeneous, anisotropic domain is presented next.

Flow in Heterogeneous Anisotropic Domain

In this experiment, we explore the flow behavior due to heterogeneity in conductivity and in anisotropy. The domain considered is a 1000 m (along *x*) by 800 m (along *y*) by 2 m (along *z*) cubical block. The conductivity, moisture content, and saturation relations are the same as used in the previous experiment. The initial head in the model domain is set to 0 m. The top and bottom extremes of the domain are no-flow boundaries, while the head on the left and right boundaries are held constant at 0 m and-30 m, respectively. A rectangular subdomain of dimensions 200 m (along *x*) by 160 m (along *y*) by 2 m (along *z*) exists at the center of the experimental region. The domain is decomposed into 3948 prismatic elements. We note that subdomain boundary was used as a constraint in generation of Delaunay triangulations. Figure 9 shows the decomposed domain and the conductivity properties relevant to each region. Four setups were considered: (a) soil properties in the rectangular subdomain are the same as in rest of the domain (homogeneous, anisotropic); (b) soil conductivity in the subdomain is different (lower) than in rest of the region, although the principal direction of conductivity is oriented along the model coordinates everywhere (heterogeneous, anisotropic); (c) soil conductivity is same everywhere in the region; however, the principal direction of anisotropy in the subdomain is oriented at 45-degree angle to the model coordinates (heterogeneous, phase shifted anisotropy); and (d) similar to case c, although the principal direction of conductivity in rest of the domain is oriented at 135 degrees to positive *x* direction.

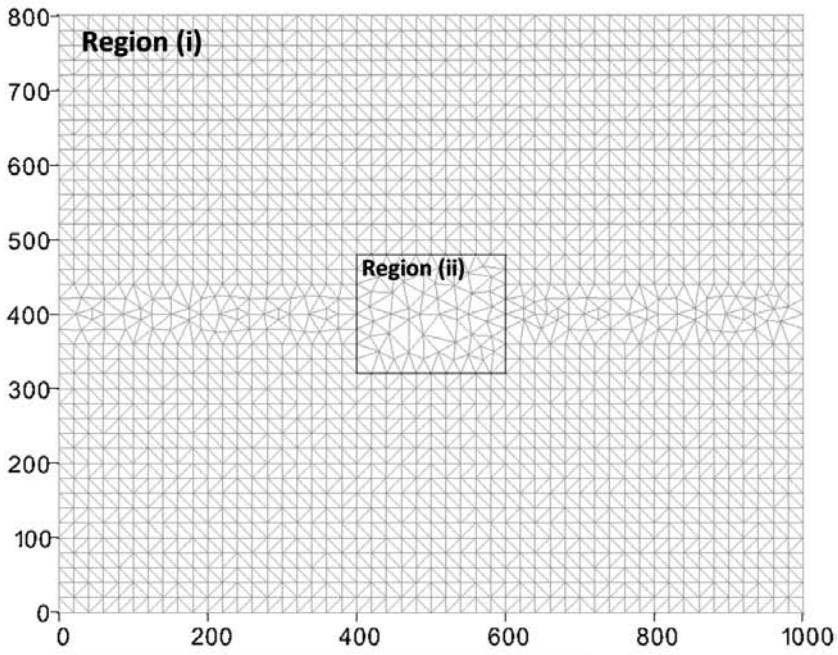

Case	Region (i)	Region (ii)
a	0.5 m/d, 20 m/d	0.5 m/d, 20 m/d
b	0.5 m/d, 20 m/d	0.5 m/d, 5 m/d
c	0.5 m/d, 20 m/d	20 m/d, 0.5 m/d, 45 ^{0}
d	0.5 m/d, - 45 ^{0}, 20 m/d	20 m/d, 0.5 m/d, 45 ^{0}

FIG. 9. Setup to study anisotropic heterogeneous flow. Four subsurface flow experiments were explored by setting the hydraulic conductivity and its orientation in region (i) and region (ii) to be different. The domain is discretized into 3948 prismatic elements. The boundary for region (ii) has been used as a constraint in generation of triangles.

Results of simulation for each case are shown in Fig. 10. Figure 10a shows a uniform variation in head from left to right boundaries. Due to the introduction of heterogeneity by a low conducting rectangular subdomain, the contour intervals within the subdomain are contracted (Fig. 10b). This is expected as the larger head gradient in the subdomain ensures mass balance even though its conductivity is lower than rest of the domain. Figure 10c shows the modification of head due to the change in principal axes orientation of anisotropy in the subdomain. The head contours inside the subdomain are oriented in direction of preferred conductivity, at an angle of 45 degrees clockwise to the *x* axis. Figure 10d shows a more complex case with the anisotropy in rest of the domain being rotated in a counter-clockwise direction such that the principal axes of anisotropy in the two regions are orthogonal to each other. This leads to formation of convergence (at the lower interface of subdomain) and divergence (at the upper interface of subdomain) zones in the flow domain. This

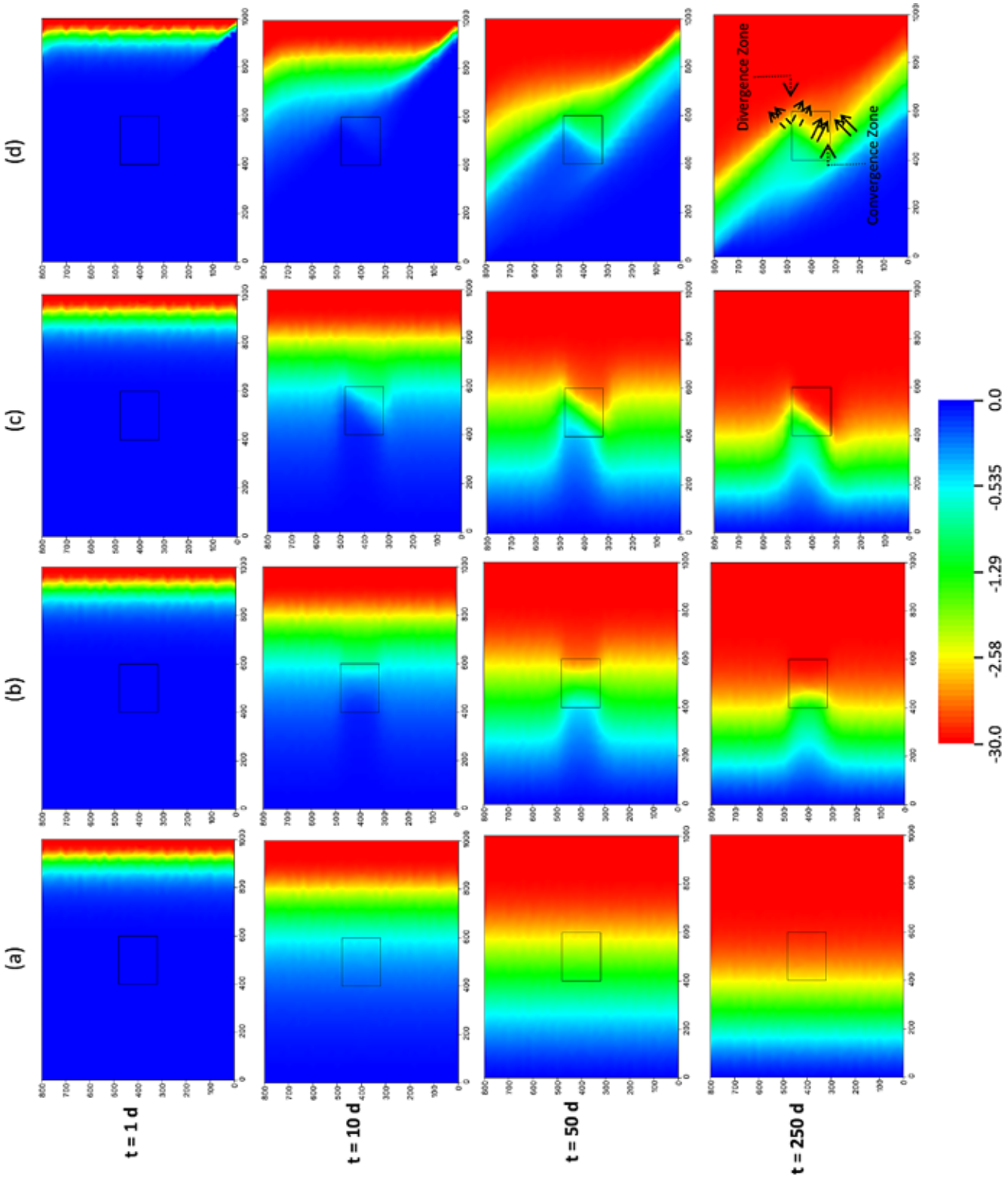

FIG. 10. Transient subsurface flow in an anisotropic heterogeneous domain. The details regarding conductivity configuration for four cases considered are shown in Fig. 9. *t* = time.

is particularly significant and shows how preferred conductivity directions might affect the contaminant mixing/spreading in a region. The shortest (case a) and longest (case d) execution times were 383 and 626 s, respectively.

Transient Three-Dimensional Variably Saturated Flow

The numerical model was validated using data from an unconfined sand aquifer pumping test performed by Nwankwor et al. (1984). The 9-m-thick aquifer is assumed to be in hydrostatic equilibrium at the start of pumping test, with total head everywhere being equal to 6.7 m. The pumping well has an inner

diameter of 0.15 m with a 4 m screen located at the bottom of the aquifer. The discharge rate of 60 L min^{-1} was maintained during the entire test, which lasted 1440 min. Head values were measured using piezometers, tensiometers, and γ access tubes installed at different radial distances from the pumping well (Nwankwor et al., 1984, 1992). The saturated conductivity of the sand aquifer was equal to 6.6×10^{-5} m s^{-1} in the horizontal direction and 4.2×10^{-5} m s^{-1} vertically. The specific storage, S_s, of the aquifer is 3.2×10^{-4} m^{-1} while the porosity and residual moisture content of the sand were equal to 0.37 and 0.07, respectively. The moisture content and potentiometric head are related through the van Genuchten model (1980) as shown in Eq. [37]:

$$\theta = \theta_r + \frac{\theta_s - \theta_r}{\left[1 + (\alpha|\psi|)^n\right]^{1-1/n}} \quad [37]$$

where $\alpha = 1.9$ m^{-1} and $n = 6.095$, respectively. Unsaturated conductivity, K(θ), and moisture content, θ, were related through

$$K(\theta) = 0.007195\theta^{4.72} \quad [38]$$

Akindunni and Gillham (1992) observed that the drawdowns were insignificantly small beyond 70 m from the pumping well, and so we conservatively set the external boundary of the domain to be at a radial distance of 100 m from the well. All of this translates to a cylindrical model domain of dimension 9 m thick and an outer radius of 100 m. Taking advantage of the symmetry of the problem, for computational efficiency, we simulated only a quarter of the domain as shown in Fig. 11. The domain is discretized into a total of 6762 prismatic elements, which includes 49 layers vertically. Variable discretization thickness was used with the top 23 layers (in unsaturated zone) being 0.1 m thick, the next 18 layers (until the start of well screen) being 0.15 m thick, and the remaining 8 layers were 0.5 m thick. The outer boundary was assigned no-flux boundary condition while the boundary condition at the well (see inset in Fig. 11) was constant flux. The value of the flux through each element's edge was equal to the total flux divided by the percentage wall area. Figure 12a shows the simulated and observed drawdown curves at horizontal distances of 5 and 15 m from the pumping well and at the depth of 7 m from the surface. A good agreement between the field data and the model results is observed. We explored further to examine the significance of drainage processes above the water table on the drawdown response in unconfined aquifers. We find that the recharge gradient at the water table reaches its maximum value (Fig. 12b) during the delayed response periods (Fig. 12a). Figure 12b also shows that the increase in recharge (gradient) can be correlated with the "excess storage" when more water is stored above the water table relative to hydrostatic conditions due to the extension of the capillary zone (Akindunni and Gillham, 1992); during this period, capillary fringe thickness (at 5 m distance) is observed to be as much as 5.6% greater than before pumping. After the initial period of rapid drawdown (Fig. 12a) and concurrent development of large vertical gradient (Fig. 12b), drainage

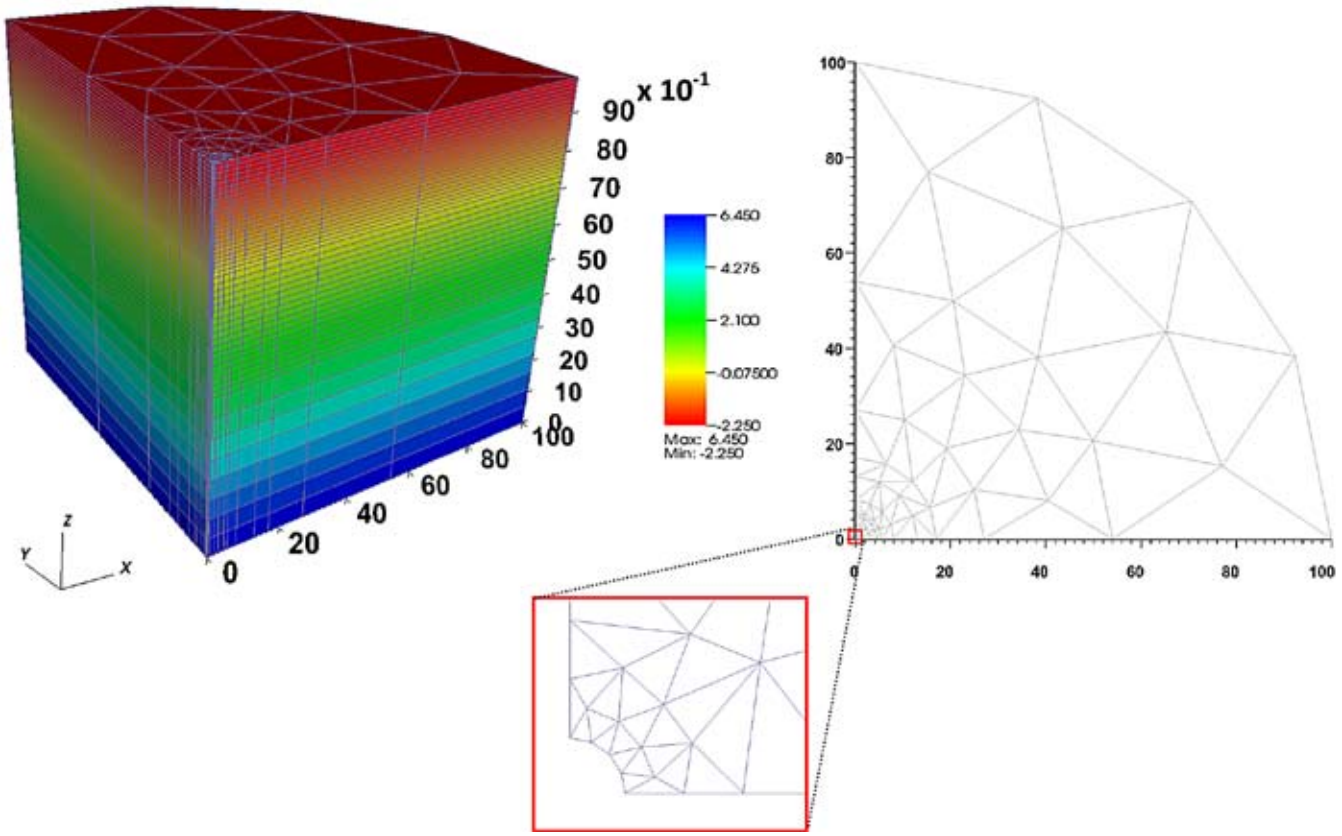

FIG. 11. Setup for validation of t variably saturated flow based on the experiment in Nwankwor et al. (1992). Due to symmetry, only one-quarter of the domain has been simulated. The initial conditions, with the water table elevation in the aquifer at 6.7 m from the bottom, are shown. The domain was discretized into 6762 elements. Well has been simulated as constant flux boundary condition applied on the inner curvilinear boundary (shown in magnified panel).

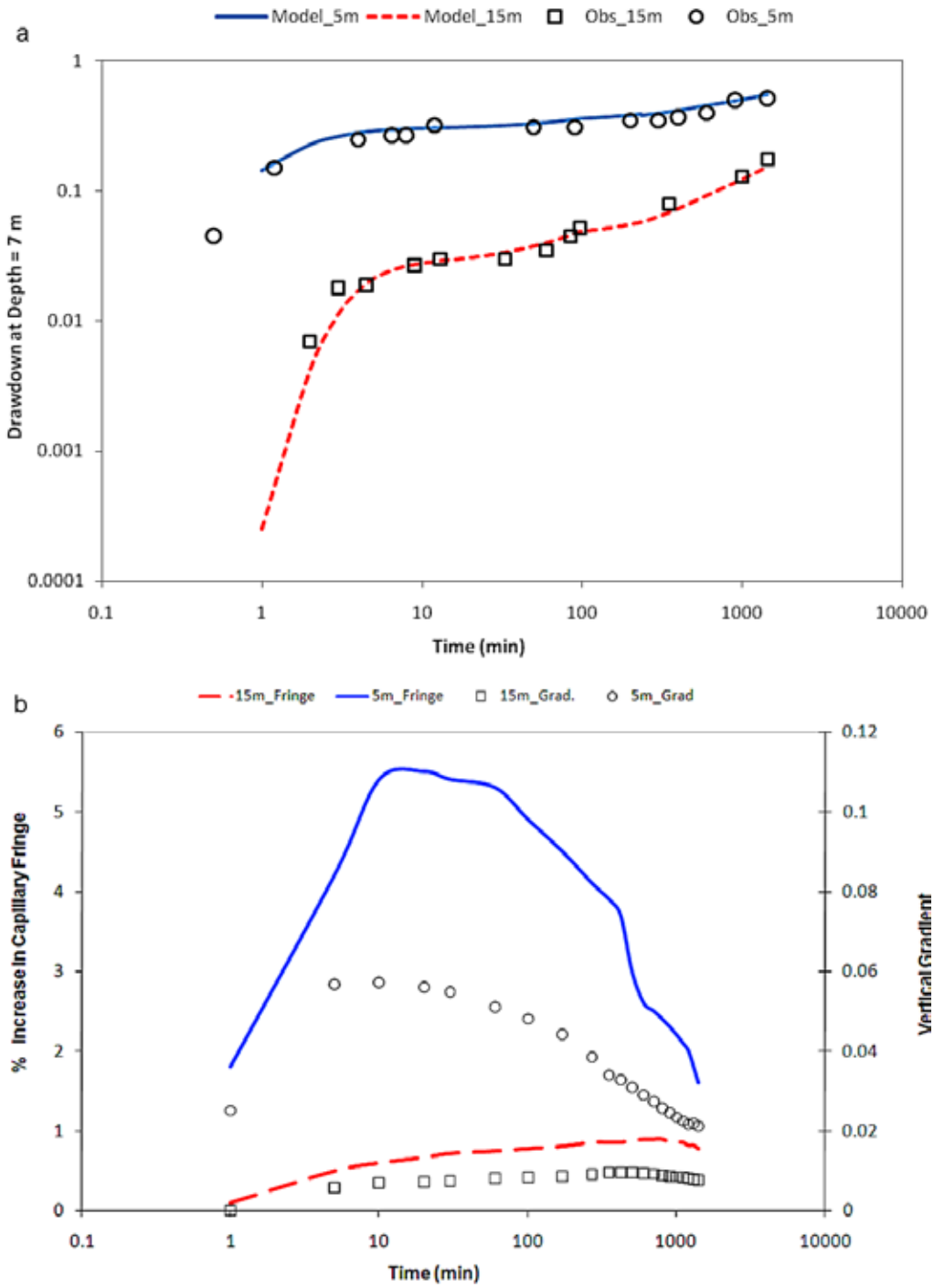

FIG. 12. (a) Drawdown (m) simulated and measured at depth 7 m from the land surface and at a radial distance of 5 (Obs_5m) and 15 m (Obs_15m) from the well casing. Observed data were obtained from Nwankwor et al. (1992). (b) Extension of capillary fringe above the water table (15m_Fringe and 5m_Fringe) and the vertical gradient (15m_Grad and 5m_Grad) at the water table at distances 15 and 5 m from the well axis. The percentage increase in the capillary fringe is relative to its thickness before pumping. Delayed yield of water from the capillary fringe is observed at times with maximum vertical gradient at the water table.

from the vadose zone reaches its maximum, yielding water to the well causing the drawdown curves to level off during the middle of the test. We also observe that the magnitude of the vertical gradient decreases with increasing distance from the well, suggesting that at large distances, flow is predominantly radial. The simulation time for the experiment was 258 min.

Coupled Surface–Subsurface Flow

Validation of coupled surface–subsurface flow was performed by simulating a laboratory experiment conducted by Abdul and Gillham (1984). The experimental setup consisted of a plexiglass tank of dimensions 140 cm (along x), 120 cm (along z), and 8 cm (along y). The tank was packed with sand of porosity = 0.34 and van Genuchten parameters α and n for wetting and drying equal to 0.024 cm^{-1} and 5, and 0.015 cm^{-1} and 8, respectively. Equation [37] was used for the soil characteristic curve. The saturated conductivity of sand was equal to 3.5×10^{-5} m s^{-1}, while the average specific yield was determined to be 0.007 (Abdul and Gillham, 1984). Sand was packed in the tank such that it formed a sloping upper surface (slope = 12°) with its toe at a height of 74 cm from the bottom (Fig. 13). The initial water table was at 74 cm. Water was applied uniformly over the surface at a rate of 0.0011945 cm s^{-1} for 20 min. A screened tube at the toe of the slope collected generated outflow. We discretized the domain into 25 layers, with the bottom six layers being of thickness 10 cm each, followed by a transition layer of 5 cm thickness

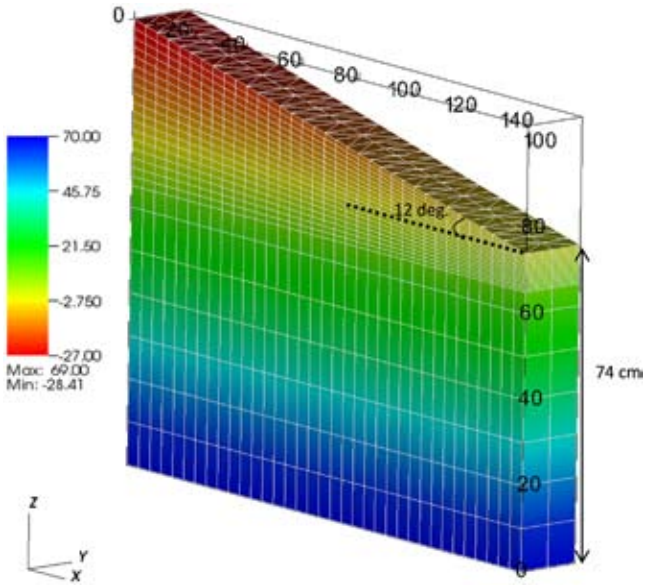

FIG. 13. Setup to study surface–subsurface flow generation using plexiglass soil column as presented in Abdul and Gillham (1984). The soil column is initially in hydrostatic equilibrium with the water table at an elevation of 74 cm from the bottom.

and then 18 prismatic layers of uniform thickness until the top. Laterally, the domain was discretized into 140 elements (shown in Fig. 13). Boundary conditions on all sides are no-flux except at the surface outlet, where it is considered to follow a critical head condition. Figure 14 shows the outflow hydrograph simulated by InHM (VanderKwaak, 1999) and FIHM for the given experimental settings (base case), and from the observations (Abdul and Gillham, 1984). The simulation time for the experiment was 25.2 min. The hydrograph shape and the peak magnitudes simulated by FIHM are consistent and closely match the observations, with a transient steady-state condition obtained after approximately 270 s. The quick response of the hillslope is due to the capillary fringe that extends almost 35 cm above the water table. Even in uphill areas where initial water table is deeper, the extended capillary fringe results in very little storage capacity in unsaturated zone. The FIHM simulation better captures the ascending and the receding limb of the hydrograph than InHM; InHM uses a different infiltration function, which may explain the differing results. Figure 15 (Case I) shows that during the initial 1200 s of simulation (time for which water is applied on the surface), infiltration occurs on the upper portion of the hillslope at the same rate as precipitation. Concurrently, as the subsurface head builds up near the toe of the hillslope, groundwater exfiltrates and contributes to the surface flow hydrograph. The portion of the hillslope discharging groundwater to the surface increases from the lowest few centimeters initially, to approximately 45% of the total hillslope during peak outflow. Even in uphill areas where initial water table is deeper, quick groundwater response is observed due to the extended capillary fringe (almost 35 cm thick above the water table), which translates to an unsaturated zone with little storage capacity. During the period of peak outflow, the exfiltration rate at the toe of the hillslope is higher than the infiltration rate anywhere on the surface. After the precipitation is stopped (Fig. 15, right panel), the remaining overland flow on the hillslope drains down while the unsaturated zone desaturates. Infiltration ceases to occur on the upper portion of the hill, while exfiltration continues at the toe. The infiltration rate peaks at the junction between dry overland and desaturated subsurface, which shifts downhill as the recession proceeds. Region upslope of the infiltration peak is dry overland, which results in zero infiltration rates. As we move downslope from the infiltration peak, both overland flow depth and potentiometric head in the underlying subsurface layer increases. However, the rate of increase of overland flow depth lags behind rate of increase of subsurface head. This leads to decrease in infiltration rate as we move down along the hillslope transect. The infiltration–exfiltration curve recedes toward a new equilibrium as the time progresses. Note that during recession (see Fig. 15), hillslope area that exfiltrates exceeds that of infiltration.

To explore the influence of initial water table (and hence, the capillary zone that extends 35 cm above the water table) on runoff generation, we simulate the previous experiment (Case I) with a reduced initial water table height of 34 cm (40 cm lower than in last experiment, Case II). The hydrograph in Fig. 14, indicates that for the initial 552 s, all the water applied to the hillslope infiltrates. Negligible infiltration–excess overland flow is produced and the infiltrated water contributes to increase in water table. Once the hillslope surface starts saturating, it results in generation of saturation–excess overland flow on the lower portion of the slope (Fig. 15). Next, we reduced the conductivity of the hillslope from 3.5×10^{-5} m s^{-1} to 1.0×10^{-7} m s^{-1} (Case III) to study the effect

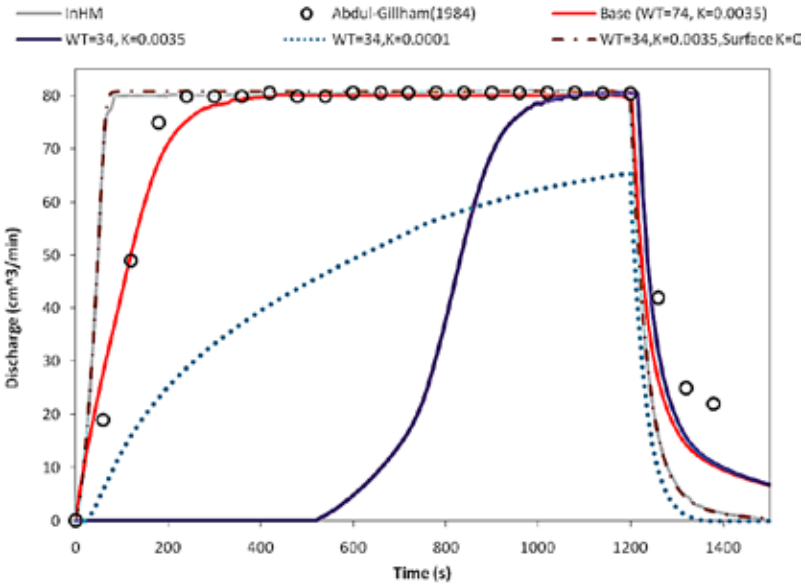

FIG. 14. Streamflow hydrograph generated at the outlet of soil column in surface–subsurface coupling experiment by Abdul and Gillham (1984). Base case corresponds to hydrograph simulated by FIHM (Case I, Base [WT = 74, K = 0.0035]) where initial water table was set at 74 cm. Three more experiments were conducted to study surface–subsurface coupling. In Case II (WT = 34, K = 0.0035), initial water table was set at 34 cm. Case III (WT = 34, K = 0.0001) has the same settings as Case II with reduced conductivity of 0.0001 cm s^{-1}. Case IV (WT = 34, K = 0.0035, surface K = 0) has a similar setting as Case II, but the surface was made impermeable. WT = water table elevation, and K = saturated conductivity (in cm/s^{-1}).

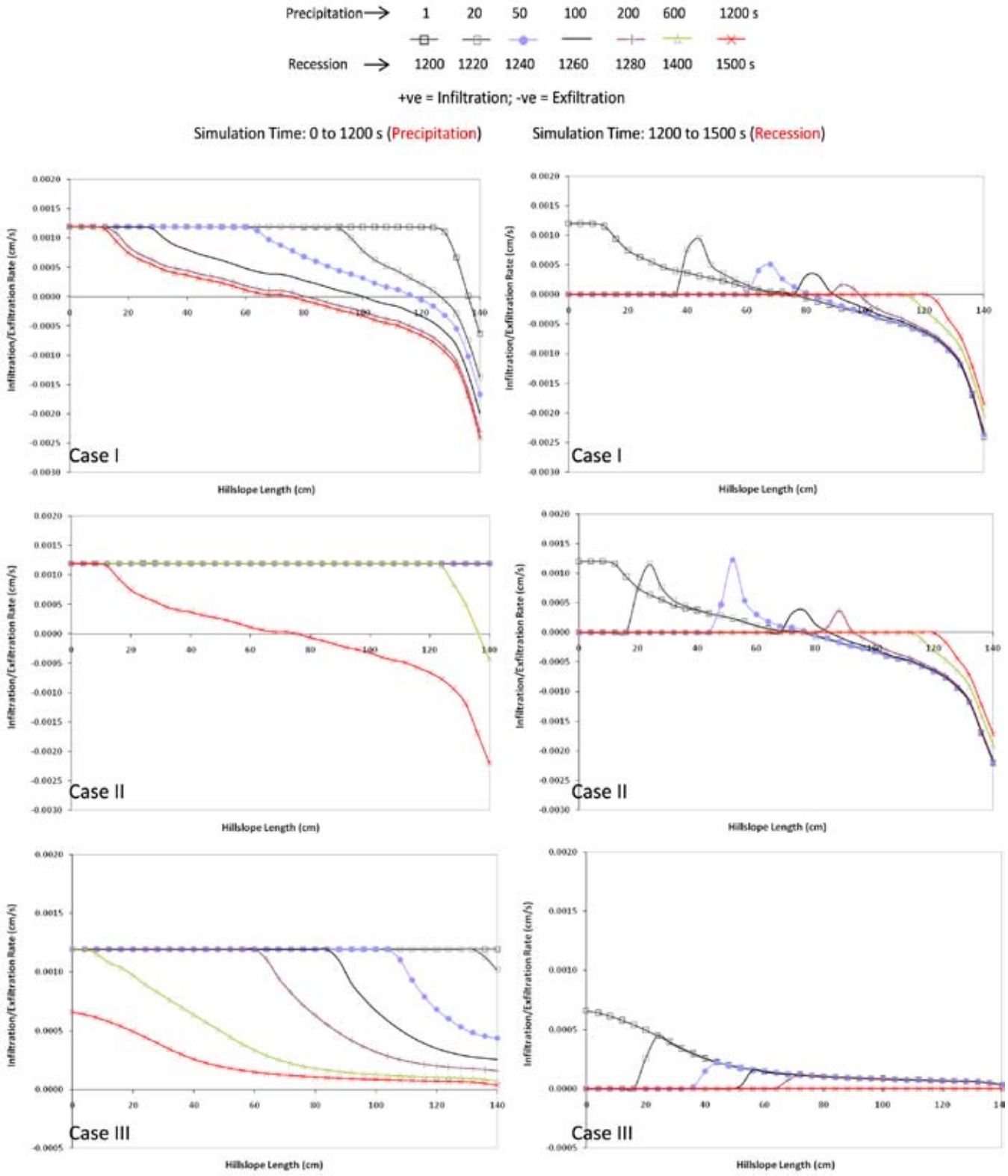

FIG. 15. Infiltration–exfiltration rate along the length of the hillslope. Four experiments each highlighting the influence of capillarity (Case I), initial water table height (Case II), conductivity, and infiltration excess runoff (Case III and IV) were conducted to study the coupling between surface and subsurface processes. Case IV has zero infiltration–exfiltration rate at all times. Left panels are for the precipitation period (through 1200 s); right panels are for the period after rainfall ceases (1200–1500 s).

of physiographic properties on runoff generation. The reduced conductivity resulted in generation of infiltration–excess overland flow, right from the start of the simulation (see Fig. 14). Because of the lower conductivity, the rate of water table increase is slower and so the surface of the hillslope never saturates. However, the persistent increase in subsurface saturation during this period (first 1200 s) still influences the infiltration rate. As observed in Fig. 15, infiltration rate decreases monotonically toward the toe

of the hill slope where a higher subsurface saturation is expected. In the last experiment (Case IV), we used experimental settings similar to Case II, the only change being setting the top surface conductance to be equal to zero (impervious). As expected, the outflow produced in this case is entirely due to infiltration–excess runoff, as neither infiltration nor exfiltration can occur along the hillslope. The corresponding hydrograph is shown in Fig. 14. This set of coupled surface–subsurface experiments shows that vadose zone capillarity, initial position of groundwater table, soil properties, and topography play important roles in the generation of surface runoff. The infiltration to the groundwater is observed to be equally dependent on these critical flow, material and topographic parameters.

Conclusions

A second-order accurate, finite volume framework to understand and predict coupled surface and subsurface flow is presented. The model simulates a full three-dimensional solution for saturated–unsaturated flow in the subsurface and a two-dimensional solution for overland runoff on the surface. Using a set of six experiments, we show the influence of soil heterogeneity, anisotropy, and topography on the distribution of moisture above and below the ground surface. The capability of the integrated model to simulate flow behavior in heterogeneous, anisotropic materials shows the possible development of local "flux rotation" phenomena. The experiments also underscore the degree to which detailed coupled surface–subsurface physics can be studied, such as where runoff generation and infiltration become closely coupled to underlying groundwater levels and adjacent surface water states. The model takes advantage of constrained Delaunay triangulation for domain discretization, which is also supported by a "shared data model," leading to accurate representation of data and fast prototyping of model experiments. The test cases presented were chosen not only to compare individual model components against classical examples from the literature (e.g., one-dimensional unsaturated flow or two-dimensional surface flow) but also to further examine the degree to which individual unsaturated–saturated zone flow or surface–subsurface processes are affected by each other. Representative experiments explored in detail the influence of drainage from unsaturated zone on delayed water table drawdown during pumping, the role of water table position on infiltration and surface runoff, and the interaction of overland flow–unsaturated zone–groundwater exchanges in relation to the dynamics of infiltrating–exfiltrating surfaces on the hillslopes.

Appendix

An alternative derivation of the normalized flux can be obtained by calculating gradients in a local coordinate system ($x1$, $y1$) that is oriented along the principal directions of anisotropy (see Fig. 4); θ is the angle of orientation of ∇h to the global x axis:

$$\begin{aligned}\vec{n}\cdot\vec{F} &= (K_1\nabla h_{x_1}\hat{i}_1 + K_2\nabla h_{y_1}\hat{j}_1)\cdot\vec{n}\\ &= \left[K_1\nabla h\mathrm{Cos}(\theta-\beta)\hat{i}_1 + K_2\nabla h\mathrm{Sin}(\theta-\beta)\hat{j}_1\right]\cdot\vec{n}\\ &= \left[K_1\nabla h\mathrm{Cos}(\theta-\beta)\mathrm{Cos}(\alpha-\beta) + K_2\nabla h\mathrm{Sin}(\theta-\beta)\mathrm{Sin}(\alpha-\beta)\right]\\ &= \left[K_1\mathrm{Cos}(\theta-\beta)\mathrm{Cos}(\alpha-\beta) + K_2\mathrm{Sin}(\theta-\beta)\mathrm{Sin}(\alpha-\beta)\right]\nabla h\end{aligned} \quad [A1]$$

Note that the normalized lateral flux expression obtained in Eq. [30] and Eq. [A1] is the same.

References

Abdul, A.S., and R.W. Gillham. 1984. Laboratory studies of the effects of the capillary fringe on streamflow generation. Water Resour. Res. 20:691–698.

Akindunni, F.F., and R.W. Gillham. 1992. Unsaturated and saturated flow in response to pumping of an unconfined aquifer: Numerical investigation of delayed drainage. Ground Water 30:873–884.

Barrash, W., and M.E. Dougherty. 1997. Modeling axially symmetric and nonsymmetric flow to a well with MODFLOW, and application to Goddard2 well test, Boise, Idaho. Ground Water 35:602–611.

Bear, J. 1975. Dynamics of fluids in porous media. Elsevier, New York.

Bermudez, A., and M.E. Vazquez. 1994. Upwind methods for hyperbolic conservation laws with source terms. Comput. Fluids 23:1049–1071.

Bertolazzi, E., and G. Manzini. 2004. A cell-centered second-order accurate finite volume method for convection–diffusion problems on unstructured meshes. Math. Models Methods Appl. Sci. 8:1235–1260.

Blazek, J. 2001. Computational fluid dynamics: Principles and applications. Elsevier Science, Amsterdam.

Brooks, R.H., and A.T. Corey. 1966. Properties of porous media affecting fluid flow. J. Irrig. Drain. Div. 92(IR2):61–88.

Brown, P.N., and A.C. Hindmarsh. 1989. Reduced storage matrix methods in stiff ODE systems. J. Appl. Math. Comput. 31:49–91.

Byrne, G.D., and A.C. Hindmarsh. 1975. A polyalgorithm for the numerical solution of ordinary differential equations. ACM Trans. Math. Softw. 1(1):71–96.

Cohen, S.D., and A.C. Hindmarsh. 1994. CVODE user guide. Technical Rep. UCRL-MA-118618. Lawrence Livermore National Lab., Livermore, CA.

Di Giammarco, P., E. Todini, and P. Lamberti. 1996. A conservative finite elements approach to overland flow: The control volume finite element formulation. J. Hydrol. 175:267–291.

Discacciati, E.M.M., and A. Quarteroni. 2002. Mathematical and numerical models for coupling surface and groundwater flows. Appl. Numer. Math. 43:57–74.

Fiedler, F.R., and J.A. Ramirez. 2000. A numerical method for simulating discontinuous shallow flow over an infiltrating surface. Int. J. Numer. Methods Fluids 32:219–240.

Frink, N.T. 1994. Recent progress towards a three-dimensional unstructured Navier–Stokes flow solver. AIAA Pap. 94-0061. Am. Inst. of Aeronautics and Astronautics, Washington, DC.

Frink, N.T., and S.Z. Pirzadeh. 1999. Tetrahedral finite-volume solutions to the Navier–Stokes equations on complex configurations. Int. J. Numer. Methods Fluids 31:175–187.

Gottardi, G., and M. Venutelli. 1993. A control-volume finite-element model for two-dimensional overland flow. Adv. Water Resour. 16:277–284.

Graham, D.N., and A. Refsgaard. 2001. MIKE SHE: A distributed, physically based modeling system for surface water/groundwater interactions. p. 321–327. *In* S. Seo, E.P. Poeter, C. Zheng, and O. Poeter (ed.) MODFLOW 2001 and Other Modeling Odysseys: Conference Proceedings, Golden, CO. 11–14 Sept. 2001. Int. Groundwater Modeling Center, Golden, CO.

Haverkamp, R., R.M. Vauclin, J. Touma, P.J. Wierenga, and G. Vachaud. 1977. A comparison of numerical simulation models for one-dimensional infiltration. Soil Sci. Soc. Am. J. 41:285–294.

Holmes, D.G., and S.D. Connell. 1989. Solution of the 2D Navier–Stokes equations on unstructured adaptive grids. p. 25–39. *In* Proc. of the AIAA Computational Fluid Dynamics Conf., 9th, Buffalo, NY. 13–15 June 1989. Am. Inst. of Aeronautics and Astronautics, Washington, DC.

Hubbard, M.E. 1999. Multidimensional slope limiters for MUSCL type finite volume schemes on unstructured grids. J. Comput. Phys. 155:54–74.

Huyakorn, P.S., and G.F. Pinder. 1983. Computational methods in subsurface flow. Academic Press, New York.

Jackson, K.R., and R. Sacks-Davis. 1980. An alternative implementation of variable step-size multistep formulas for Stiff ODEs. ACM Trans. Math. Softw. 6:295–318.

Jawahar, P., and H. Kamath. 2000. A high-resolution procedure for Euler and Navier–Stokes computations on unstructured grids. J. Comput. Phys. 164:165–203.

Kim, S.E., B. Makrov, and D. Caraeni. 2003. A multi-dimensional linear reconstruction scheme for arbitrary unstructured grids. *In* Proc. of the 16th AIAA Computational Fluid Dynamics Conf., 16th, Orlando, FL. 23–26 June 2003. Am. Inst. of Aeronautics and Astronautics, Washington, DC.

Kollet, S.J., and R.M. Maxwell. 2006. Integrated surface-groundwater flow modeling: A free-surface overland flow boundary condition in a parallel groundwater flow model. Adv. Water Resour. 29:945–958.
Kumar, M. 2009. Towards a hydrologic modeling system. Ph.D. diss. The Pennsylvania State Univ., University Park.
Kumar, M., G. Bhatt, and C. Duffy. 2009. An efficient domain decomposition framework for accurate representation of geodata in distributed hydrologic models. Int. J. Geographical. Inf. Sci. 23 (in press).
Leake, S.A., and D.V. Claar. 1999. Procedures and computer programs for telescopic mesh refinement using MODFLOW. Open File Rep. 99-238. USGS, Tucsan, AZ.
Lin, G.F., J.S. Lai, and W.D. Guo. 2003. Finite-volume component-wise TVD schemes for 2D shallow water equations. Adv. Water Resour. 26:861–873.
Manzini, G., and S. Ferraris. 2004. Mass-conservative finite volume methods on 2-D unstructured grids for the Richards equation. Adv. Water Resour. 27:1199–1215.
Mehl, S., and M.C. Hill. 2004. Three-dimensional local grid refinement method for block-centered finite-difference groundwater models using iteratively coupled shared nodes: A new method of interpolation and analysis of errors. Adv. Water Resour. 27:899–912.
Mualem, Y. 1976. A new model for predicting the hydraulic conductivity of unsaturated porous media. Water Resour. Res. 12:513–522.
Nwankwor, G.I., J.I. Cherry, and R.W. Gillham. 1984. A comparative study of specific yield determinations for a shallow sand aquifer. Ground Water 22:764–772.
Nwankwor, G.I., R.W. Gillham, G. van der Kamp, and F.F. Akindunni. 1992. Unsaturated and saturated flow in response to pumping of an unconfined aquifer: Field evidence of delayed drainage. Ground Water 30:690–700.
Ollivier-Gooch, C., and M. Van Altena. 2002. A high-order-accurate unstructured mesh finite-volume scheme for the advection–diffusion equation. J. Comput. Phys. 181:729–752.
Panday, S., and P.S. Huyakorn. 2004. A fully coupled physically-based spatially-distributed model for evaluating surface/subsurface flow. Adv. Water Resour. 27:361–382.
Pasdunkorale, J.A., and I.W. Turner. 2003. A second order finite volume technique for simulating transport in anisotropic media. Int. J. Numer. Methods Heat Fluid Flow 13:31–56.
Qu, Y., and C.J. Duffy. 2007. A semi-discrete finite volume formulation for multi-process watershed simulation. Water Resour. Res. 43:W08419.
Shewchuk, J.R. 1996. Triangle: Engineering a 2D quality mesh generator and Delaunay triangulator. Appl. Comput. Geom. Towards Geometric Eng. 1148:203–222.
Srivastava, R., and T.J. Yeh. 1991. Analytical solutions for one dimensional, transient infiltration toward the water table in homogeneous and layered soils. Water Resour. Res. 27:753–762.
Turkel, E. 1985. Accuracy of schemes with nonuniform meshes for compressible fluid flows. Rep. 85-43. Inst. for Computer Applications in Science and Engineering, Natl. Aeronautics Space Admin., Hampton, VA.
USEPA. 1994. A technical guide to ground-water model selection at sites contaminated with radioactive substances. EPA/402/R-94/012. Office of Solid Waste and Emergency Response, USEPA, Washington, DC.
VanderKwaak, J.E. 1999. Numerical simulation of flow and chemical transport in integrated surface–subsurface hydrologic systems. Ph.D. diss. Univ. of Waterloo, Ontario, Canada.
van Genuchten, M.Th. 1980. A closed-form equation for predicting the hydraulic conductivity of unsaturated soils. Soil Sci. Soc. Am. J. 44:892–898.
Weiyan, T. 1992. Shallow water hydrodynamics. Elsevier Oceanography Series Vol. 55. Elsevier, Amsterdam.
Winter, T., J. Harvey, O. Franke, and W. Alley. 1998. Ground water and surface water: A single resource. Circ. 1139. USGS, Denver, CO.
Yeh, G.T., and J.R. Cheng. 1994. 3DFEMWATER user manual: A three-dimensional finite-element model of water flow through saturated-unsaturated media. Version 2.0. Pennsylvania State Univ., University Park.
Yeh, G.T., and G.B. Huang. 2003. A numerical model to simulate water flow in watershed systems of 1-D stream-river network, 2-D overland regime, and 3-D subsurface media (WASH123D: Version 1.5). Dep. of Civil and Environmental Engineering, Univ. of Central Florida, Orlando.

Executive Summary

A physics-based, fully coupled, constrained unstructured grid-based hydrologic model is presented. The model explores the influence of initial hydrologic states, soil properties, capillarity, anisotropy and heterogeneity in determining the hydrologic coupling behavior between the surface, the vadose, and saturatedzones.